JOURNAL OF GEOPHYSICAL RESEARCH, VOL. 106, NO. C11, PAGES 26,959–26,984, NOVEMBER 15, 2001

Modeling studies of the coastal circulation off northern California: Statistics and patterns of wintertime flow

Julie Pullen[1] and J. S. Allen

College of Oceanic and Atmospheric Sciences, Oregon State University, Corvallis, Oregon, USA

Abstract. We conduct modeling studies of the coastal circulation off northern California in the vicinity of the Eel River (40.6°N, the site of the 1995-2000 Strata Formation on Margins (STRATAFORM) marine geology observational program) using a series of nested hydrostatic primitive equation models to aid in the understanding of the shelf flow field that receives and transports sediments during the winter floods. The basic objectives of our numerical studies are to model the continental shelf and slope flow and to understand the dominant dynamical processes. We simulate the shelf and slope flow surrounding Cape Mendocino during 100 days in winter 1996–1997 using a 3 km resolution model embedded in a 9 km resolution regional model of the North Pacific Ocean (the Naval Research Laboratory's Pacific West Coast (PWC) model). The validity of the model simulations is assessed by comparison with current measurements from a STRATAFORM shelf tripod outfitted with an acoustic Doppler current profiler and with satellite altimetry. Good agreement is found between the amplitude and time variability of the 3 km resolution modeled and observed alongshore currents on the shelf. The 3 km resolution model outperforms the 9 km resolution PWC model. Using statistical maps of flow variables, strong alongshore variability in wintertime flow is documented. The role of the forcing supplied by wind and river runoff in establishing this flow asymmetry between regions north and south of Cape Mendocino is examined using empirical orthogonal functions. The evolution of a robust anticyclonic eddy over the shelf and slope adjacent to Cape Mendocino is described. The eddy forms when strong poleward winds weaken and reverse direction during winter storms. The important role of alongshore pressure gradients in the shelf circulation is documented.

1. Introduction

Atmospheric circulation during winter over northern California is dominated by large low-pressure systems with length scales of hundreds of kilometers that pound the coastal region. Maximum wind variability is typically found north of Cape Mendocino, with variability decreasing to the south of the cape [*Halliwell and Allen,* 1987; *Strub et al.,* 1987]. The veering of storm-derived winds is a major forcing mechanism for northern California winter oceanic circulation over the shelf [*Largier et al.,* 1993]. In addition to generating significant variability in wind forcing, the storms deliver precipitation to the coastal mountain range. The fresh water is transported rapidly to the coastal ocean by rivers. The resultant river runoff is a source of buoyancy that provides an additional forcing mechanism for the circulation on the northern California shelf.

The winter season of 1996–1997 contained several major storm events. One severe storm produced a massive Eel River flood with a recurrence time of 80 years [*Syvitski and Morehead,* 1999]. Indeed, winter 1996–1997 contained a confluence of forcing factors that enriched the circulation around Cape Mendocino. The major storms that generated intense winds and caused significant flooding of northern California rivers augmented the complexity of the circulation already complicated by tortuous bathymetry and sharp coastline curvature at Cape Mendocino.

The shelf and slope region surrounding Cape Mendocino was heavily instrumented as part of the Northern California Coastal Circulation Study (NCCCS), 1987–1989 [*EG&G, Inc.,* 1991]. The goal of that study was to describe seasonal patterns of alongshore variability over the shelf and slope off northern California. The observation period contained one winter (1988–1989). More recently, since 1995 the Strata Formation on Margins

[1]Now at Marine Meteorology Division, Naval Research Laboratory, Monterey, California, USA.

Paper number 2000JC000548.
0148-0227/01/2000JC000548$09.00

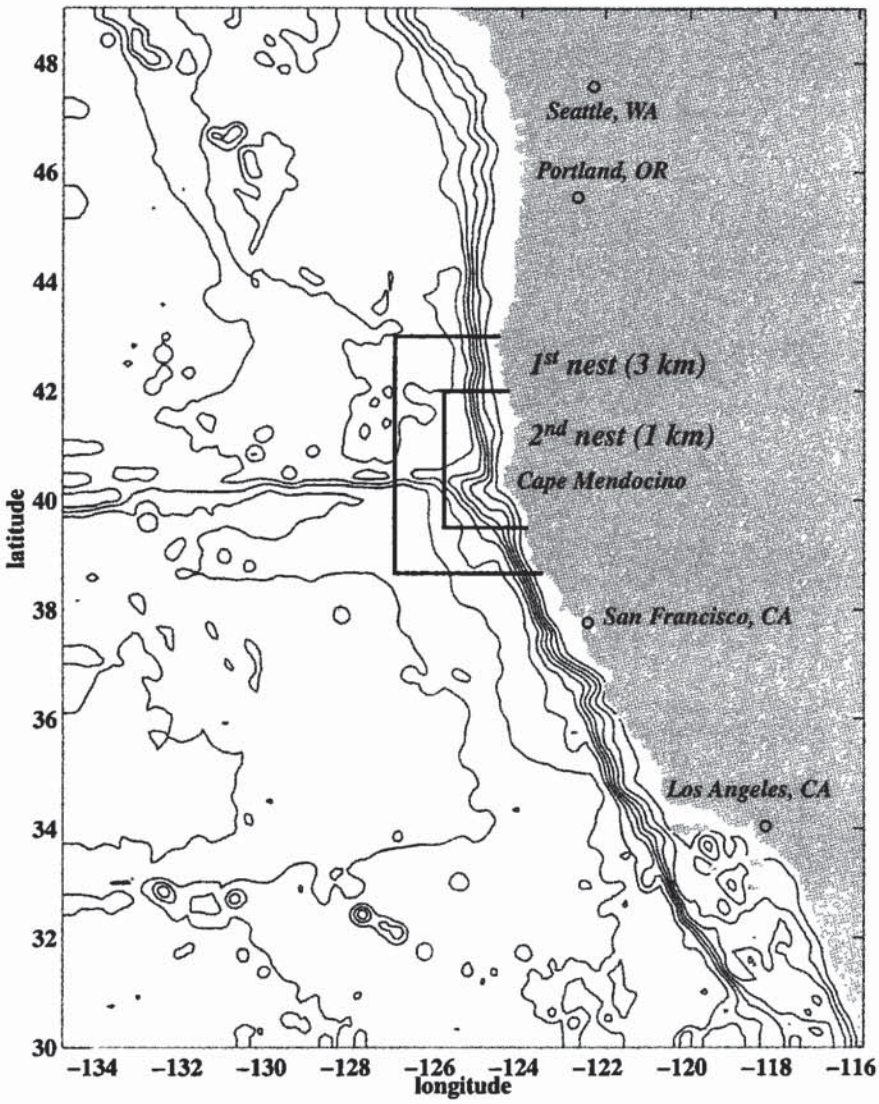

Figure 1. Model domain and bathymetry of the NRL's PWC model. The bathymetry contour interval is 500 m. Boundaries of the nested models are indicated.

(STRATAFORM) observational program has collected data in the region north of Cape Mendocino [*Nittrouer*, 1999]. A goal of that program is to understand the formation of shelf stratigraphy by deposition of sediments from the Eel River. Sediment deposition is intensified during winter floods, so instrument deployment is focused around these times. Physical measurements include moorings over the shelf and slope outfitted with current meters and temperature/salinity sensors, as well as two tripods on the shelf instrumented with acoustic Doppler current profilers (ADCPs). Though much is known about the northern California shelf and slope region from the analysis of observations during spring and summer upwelling (e.g., *Largier et al.* [1993] and the Coastal Ocean Dynamics Experiment (CODE) as described by *Beardsley and Lentz* [1987]) winter circulation has only recently received attention [*Dever*, 1997a; *Lentz and Trowbridge*, 2001].

Reflecting the focus of observational efforts, spring and summer upwelling conditions off the U.S. west coast have been modeled at high (<5 km) resolution [*Oey*, 1996; J. Gan and J. S. Allen, Model studies of shelf circulation off northern California in the region of the Coastal Ocean Dynamics Experiment: Part 1, response to relaxation of upwelling winds, submitted to *Journal of Geophysical Research*, 2000; Oke et al., Assimilation of surface velocity data into a primitive equation coastal ocean model, submitted to *Journal of Geophysical Research*, 2000]. However, the winter season has not been the subject of realistic high-resolution modeling studies. In addition, the coastal ocean surrounding Cape Mendocino has not previously been investigated in a modeling study. The numerical study described here constitutes a realistic simulation of winter 1996–1997 flow conditions in the vicinity of Cape Mendocino by including accurate representation of the major forc-

ing mechanisms: wind stress, river runoff, open ocean variability, and flow interaction with coastline curvature and bathymetry.

The finite difference numerical model, domain, forcing, and nesting method are described in sections 2 and 3. Statistics over several winter months of the 3 km nested model simulation are analyzed in section 4 in order to characterize the large alongshore scale (order 100 km) spatial properties of the coastal flow north and south of Cape Mendocino as well as the influence of river runoff on shelf circulation. The nature of fluctuations over the shelf is described by analyzing model results on across-shelf sections. Next we focus on the highly variable region north of Cape Mendocino, which was instrumented by the STRATAFORM program. Model time series at a site on the shelf are compared with the observed time series in section 5. Dynamical balances are presented for that location. Finally, we identify robust eddy formation generated in response to the passage of intense storms in section 6. Results are discussed and summarized in section 7.

2. Model Configuration

The Naval Research Laboratory (NRL) has developed a model to reproduce the seasonal circulation off the U.S. west coast [*Clancy et al.*, 1996]. The Pacific West Coast (PWC) model is a version of the stratified hydrostatic primitive equation Princeton Ocean Model [*Blumberg and Mellor*, 1987]. The simulation domain comprises the North Pacific Ocean from 30° to 49°N and from 135°W to the west coast (Figure 1). The domain is represented at 1/12° (about 9 km) horizontal resolution and has 30 vertical sigma levels. Navy Digital Bathymetric Data Base (DBDB) 5' (~8 km resolution) bathymetry is used. At the open boundaries the model is coupled by a one-way nest to the six-layer finite depth 1/6° global Navy Layered Ocean Model (NLOM) [*Wallcraft*, 1991]. At NRL the PWC model was spun up for 2 years then forced with Navy Operational Global Atmospheric Prediction System (NOGAPS) [*Hogan and Rosmond*, 1991] wind stress from 1992 to 1998.

Two one-way nested grids have been configured in the PWC model (Figure 1). The first nested grid extends ~200 km offshore (from the coast to 127.1°W) and 475 km alongshore (38.6° to 43°N) and has about 3 km horizontal resolution. The second nested grid lies within the domain of the first nested grid and extends 275 km alongshore (39.5° to 42°N) and about 125 km offshore (to 125.9°W) and has ~1 km resolution. Like the PWC model, the nested models use 30 vertical sigma levels. Higher-resolution bathymetry from the Navy database is used on both nested grids, as detailed below. Interpolation to the nested grid boundaries of horizontal velocities in transport form and surface elevation follows the conservative formulation of *Clark and Farley* [1984] as described by *Pullen* [2000]. The conservative interpolation formulation derived by *Clark and Farley* [1984] is used in order to maintain consistency of the mass fluxes in the continuity equation between the grids of differing resolution. Other scalar prognostic variables are interpolated linearly. The first nested model was initialized with PWC model fields from October 25, 1996, and subsequently run for over 100 days. The second nested model was used for a 40 day simulation of the major Eel River flood event. *Pullen and Allen* [2000] analyze the second nested model simulation of the Eel River flood event. The present paper centers on the first nested model (3 km resolution), hereinafter referred to as the "nested model" in the analysis sections.

Internal (external) time steps are 600 s (12 s) for the PWC model, 120 s (4 s) for the first nest, and 24 s (0.8 s) for the second nest. Nested grid boundary values are saved every time step from the coarser-resolution model for all prognostic variables. In order to update the boundary of the nested grids, prognostic variables are interpolated linearly in time to provide values every time step. More details of the nesting implementation are described by *Pullen* [2000].

3. Model Forcing

NOGAPS model wind stress variability over the domain of the PWC model for the 100 day simulation (Plate 1) is strongest north of 39°N and weakens to the south. Mean wind stress is oriented alongshore to the north of Cape Mendocino, while to the south, mean wind stress has an onshore orientation. NOGAPS model wind stress at National Data Buoy Center (NDBC) buoy 46030 (40.4°N, 124.5°W, hereinafter referred to as buoy 30), located adjacent to Cape Mendocino, agrees well with stress calculated from winds measured at that buoy (Figure 2) (correlation coefficient = 0.92, NOGAPS (observed) mean = 0.65 (0.46) dyne cm^{-2}, and NOGAPS (observed) standard deviation = 1.73 (1.30) dyne cm^{-2}). Wind stress from the observed wind speeds was computed using the method of *Large and Pond* [1981]. NOGAPS wind stress was used to force the PWC model as well as the two nested models. Two major storm events on December 8–17 and December 29, 1996, to January 6, 1997, are evident in the wind record. Strong poleward (downwelling favorable) winds give way to equatorward (upwelling favorable) winds as the midlatitude cyclones propagate eastward. Later analysis will concentrate on these two storm passages.

River discharge values recorded hourly by the United States Geological Survey (USGS) at stream-gaging stations and archived by the California Department of Water Resources (CDWR) were low-pass filtered (Butterworth filter with cutoff period of 3 hours) then introduced into the PWC model and interior nested models using the method of *Kourafalou et al.* [1996] (see Appendix A). Discharge measured at the Turwar station

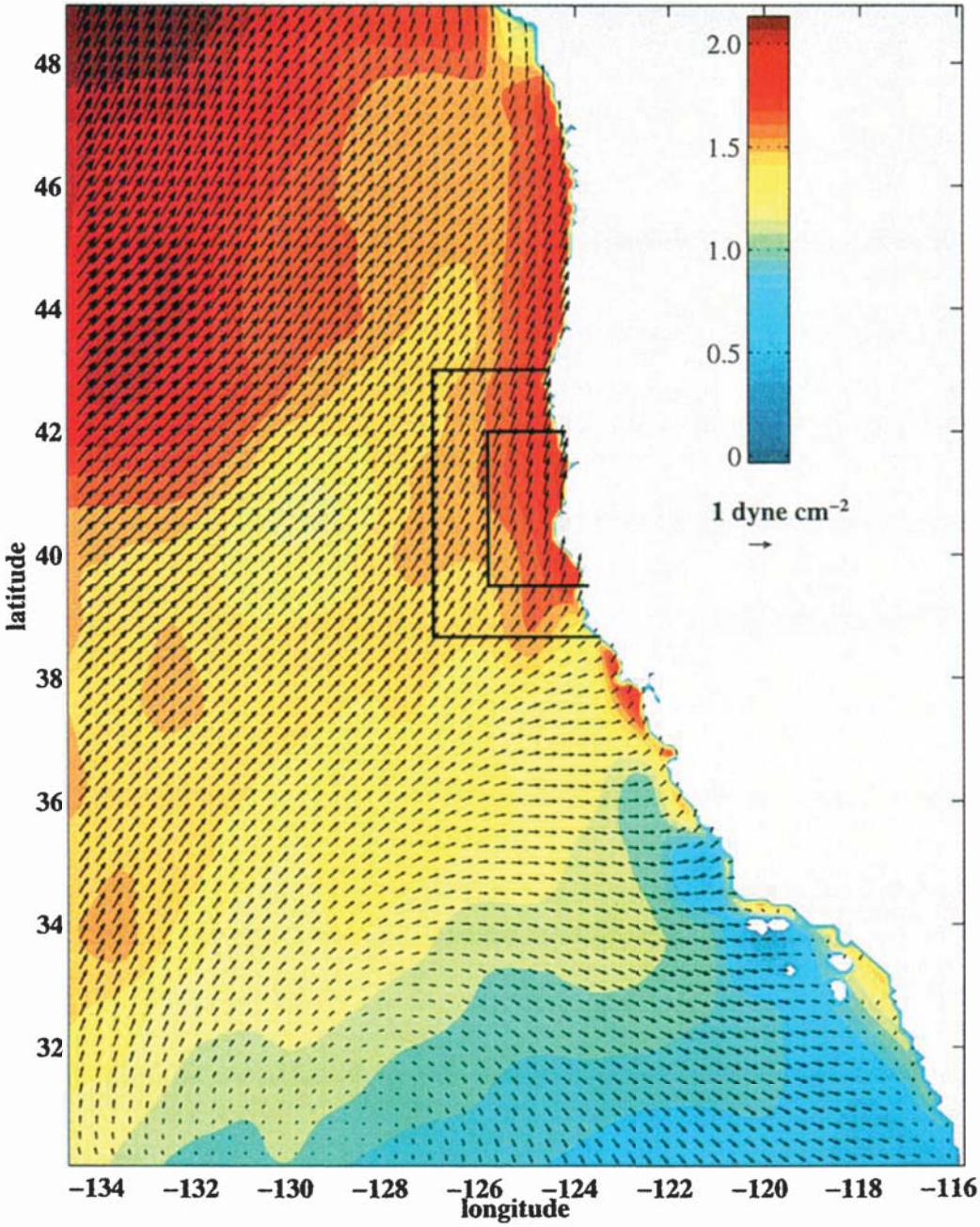

Plate 1. NOGAPS model wind stress mean and rms vector amplitude over the 100 day simulation on the PWC model domain.

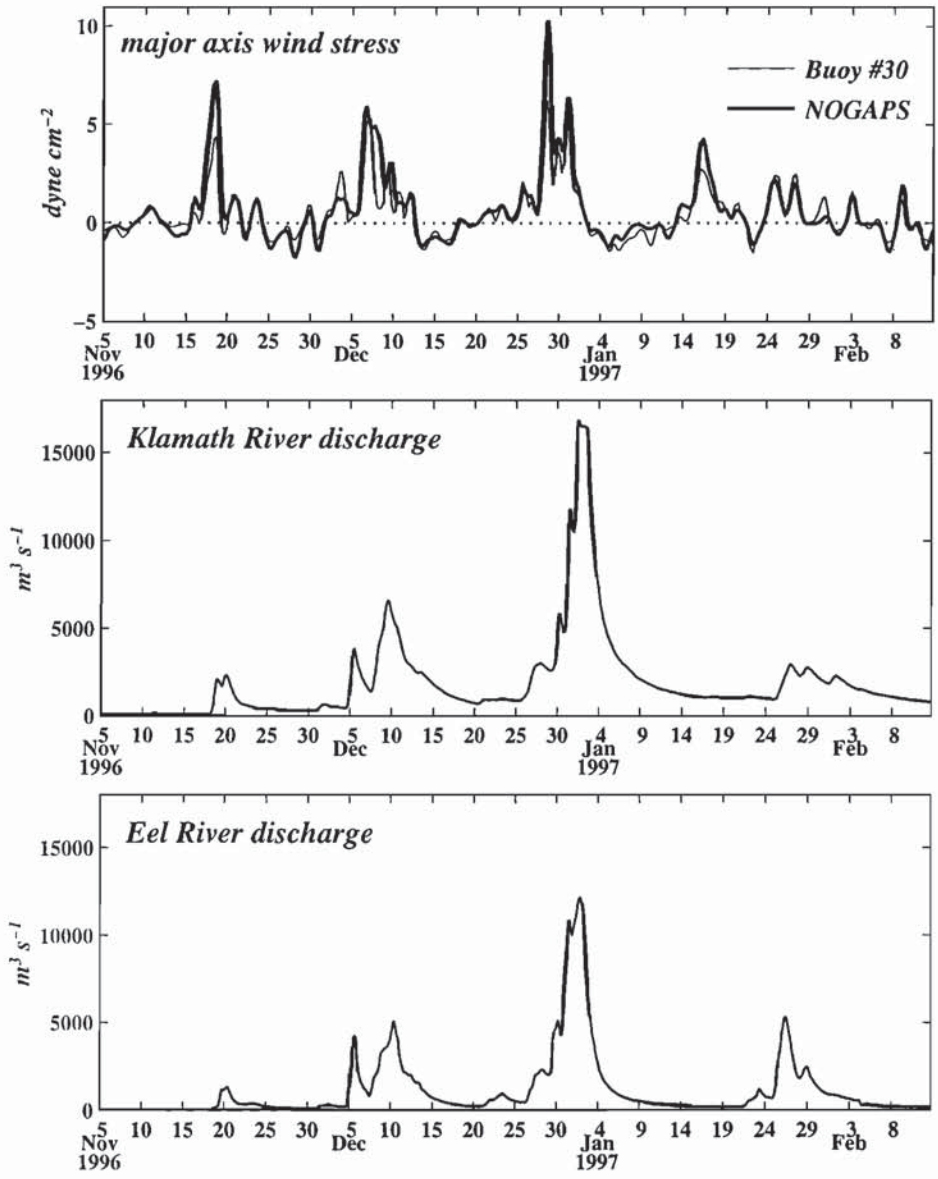

Figure 2. (top) Model forcing for the PWC and nested models for the 100 day simulation. NOGAPS model wind stress at the location of buoy 30 (40.4°N, 124.5°W) is shown along with wind stress calculated from observed wind speed at the buoy. The major axis direction for buoy 30 (NOGAPS) of -7.08° (0.41°) relative to north has been chosen. River gage discharge data for the (middle) Klamath and (bottom) Eel Rivers are also shown.

was used for the Klamath River. Discharges measured at the Scotia (Eel River) and Bridgeville (Van Duzen River) stations were combined to give discharge near the mouth of the Eel River [*Wheatcroft et al.*, 1997]. Discharge of the Rogue River was taken from climatology [*Clancy et al.*, 1996]. River runoff from both the Eel and Klamath Rivers (Figure 2) peaks as the trailing edge of the storms pass over the region around December 10 and January 2. The nested model simulation was repeated with no river runoff in order to differentiate the impact of freshwater buoyancy forcing from wind forcing on the northern California coastal circulation.

Observations from the NCCCS study suggest that mesoscale features from the open ocean can influence the shelf and slope circulation around Cape Mendocino [*Largier et al.*, 1993]. Open ocean features including jet meanders and eddies that impinge on the shelf and slope may be represented in the initialized fields from the coarser-resolution model and advected, as the simulation progresses, by a nested modeling approach.

The interaction of flow with the convoluted bathymetry around Cape Mendocino provides a final important forcing mechanism. Navy DBDB0.5' (~0.8 km) and 1' (~1.5 km) digitized bathymetry is combined to

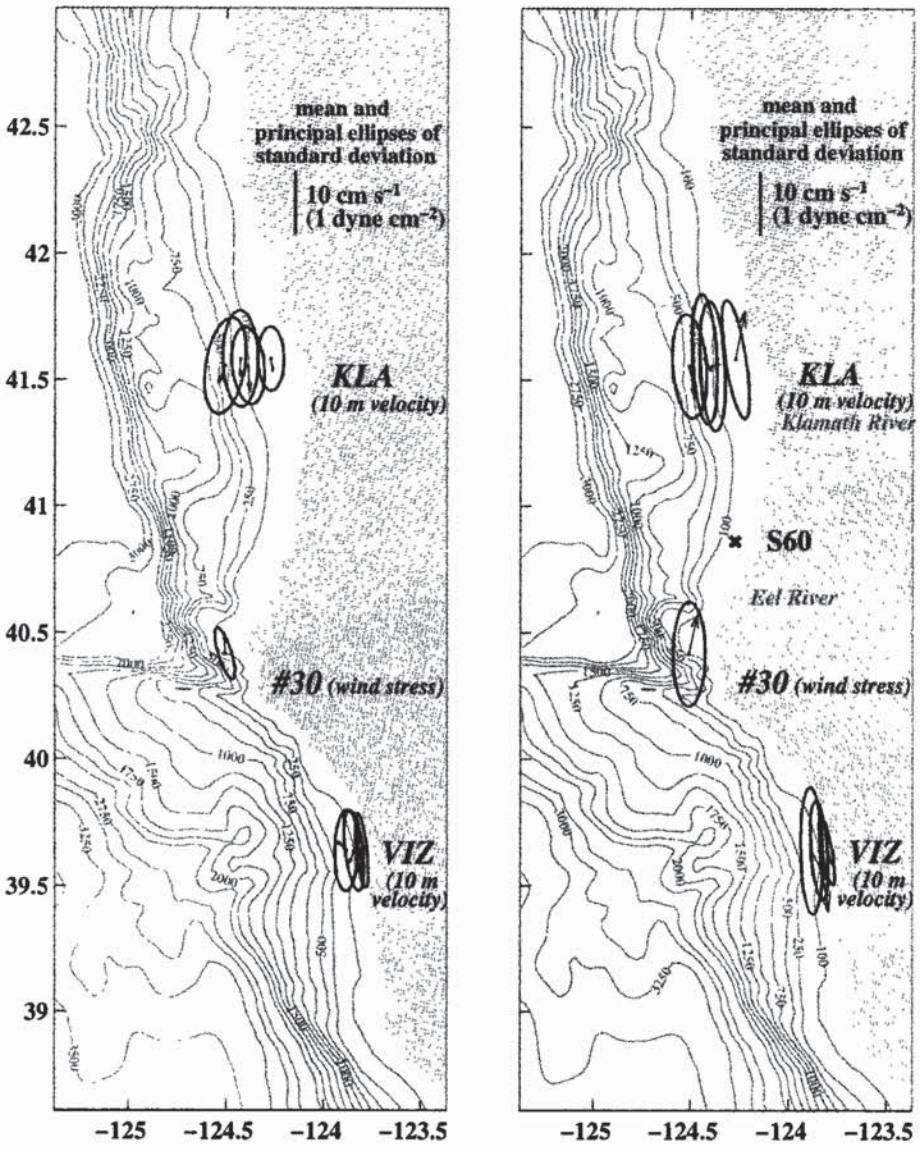

Figure 3. (left) Northern California Coastal Circulation Study (NCCCS) (November 5, 1988, to February 13, 1989) and (right) nested model (November 5, 1996, to February 13, 1997) 10 m velocity and wind stress mean and principal axis ellipses of standard deviation. Standard deviations correspond to the major axes of the ellipses. Bathymetry contours on both plots represent the actual bathymetry used on the nested model domain. The model domain is truncated to the west.

create high-resolution bathymetry for the domain inside the first nested grid boundary. Sigma coordinate models are prone to generate spurious velocities associated with pressure gradient errors near steep bathymetry [*Mellor et al.*, 1994]. In order to minimize such disturbances the bathymetry is smoothed with a Shapiro filter. The bathymetry is further manipulated to reduce the difference in adjacent depth values divided by twice the average depth of adjacent cells to be <0.4. Bathymetry on the nested grid is blended with the coarser-resolution model bathymetry over six grid cells for consistency across the nested grid boundary. Immediately off Cape Mendocino as the coastline projects westward, the bathymetry becomes highly contorted, with the Mendocino Escarpment (Figure 1) dropping sharply to the north. Furthermore, several deep submarine canyons gouge the slope area adjacent to the Cape Mendocino coast. There is a broad shelf north of Cape Mendocino, while to the south, the shelf is narrow. The high-resolution bathymetry and coastline used on the nested grid captures the important features of the coastline and underwater terrain (Figure 3).

4. Circulation Statistics

This section gives a statistical overview of the model results of the 100 day nested model (3 km resolution) simulation. Because most of the forcing mechanisms de-

Table 1. Statistics From the NCCCS Observations of Currents at 10 m Depth from November 5, 1988, to February 13, 1989[a]

Location/Isobath	Magnitude of Mean, cm s^{-1}	Direction of Mean	Standard Deviation of Major Axis, cm s^{-1}	Standard Deviation of Minor Axis, cm s^{-1}
KLA/60 m	2.17	166.87°	10.58	5.56
KLA/90 m	4.37	173.63°	12.82	6.84
KLA/130 m	3.02	182.58°	15.93	7.54
KLA/400 m	3.23	206.99°	16.16	8.20
VIZ/60 m	3.38	183.65°	12.41	2.23
VIZ/90 m	2.34	206.20°	13.42	3.77
VIZ/130 m	2.65	306.63°	13.31	5.03

[a]Orientation is given in degrees clockwise from north. Values for wind stress at buoy 30 (in dyne cm^{-2}) over the same time period are Magnitude of Mean = 0.33, Direction of Mean = 359.09°, Standard Deviation of Major Axis = 0.91, and Standard Deviation of Minor Axis = 0.27.

scribed in section 3 possess strong alongshore variability, it is natural to expect the coastal flow around Cape Mendocino to mirror this spatial inhomogeneity. This section focuses on comparing and contrasting statistical quantities at different locations in order to identify and separate the effects of the dominant physical forcings. All variables in this paper are filtered with a moving average over the 18 hour inertial period, unless otherwise stated.

As a point of departure for the analysis, current meter measurements from the NCCCS observational program are examined. The same 100 day period corresponding to the model simulation is utilized (November 5, 1996, to February 13, 1997); however, the observations are for the year 1988–1989. (It was not practical to run the nested model for the 1988–1989 period of the NCCCS experiment because the PWC simulation was conducted for 1992–1998 and NOGAPS wind forcing is not readily available for 1988–1989.) The historical NCCCS current meter data on the Klamath (KLA) and Vizcaino (VIZ) lines shown in Figure 3 and summarized in Table 1 reveal that the principal axis ellipses of standard deviation of velocity at 10 m depth are more polarized alongshore on the VIZ line (south of Cape Mendocino) compared with the KLA line (north of Cape Mendocino). The shelf is narrower at the VIZ line than at the KLA line, which can account for the observed difference in polarization. Mean flow over the shelf and slope at the KLA and VIZ lines is generally equatorward despite weak poleward mean winds.

The wind forcing during winter 1988–1989 at NDBC buoy 30 possessed a large number of equatorward wind events, leading NCCCS investigators to categorize winter 1988–1989 as anomalous [*EG&G, Inc.*, 1991]. By contrast, winter 1996–1997 displayed large mean poleward winds and higher wind variability (Figure 3). Table 2 contains the statistics from the model simulation. Model currents at 10 m depth from the present simulation (November 5, 1996, to February 13, 1997) also show stronger polarization of flow in the alongshore direction off VIZ compared to KLA. Model flow is equatorward in the mean except over the shelf on the 60 m isobath off KLA where it is poleward. The "no river" simulation also had poleward flow on the 60 m isobath at

Table 2. Statistics From the Nested Model Simulation of Currents at 10 m Depth From November 5, 1996, to February 13, 1997[a]

Location/Isobath	Magnitude of Mean, cm s^{-1}	Direction of Mean	Standard Deviation of Major Axis, cm s^{-1}	Standard Deviation of Minor Axis, cm s^{-1}
KLA/60 m	8.08	13.90°	19.99	4.29
KLA/90 m	1.61	77.43°	21.50	5.30
KLA/130 m	2.38	145.78°	21.56	5.10
KLA/400 m	5.39	165.06°	17.18	7.08
VIZ/60 m	2.65	150.63°	11.56	2.11
VIZ/90 m	10.28	169.13°	16.31	3.44
VIZ/130 m	5.83	145.63°	20.89	4.67

[a]Orientation is given in degrees clockwise from north. Values for wind stress at buoy 30 (in dyne cm^{-2}) over the same time period are Magnitude of Mean= 0.67, Direction of Mean = 15.11°, Standard Deviation of Major Axis = 1.73, and Standard Deviation of Minor Axis = 0.68.

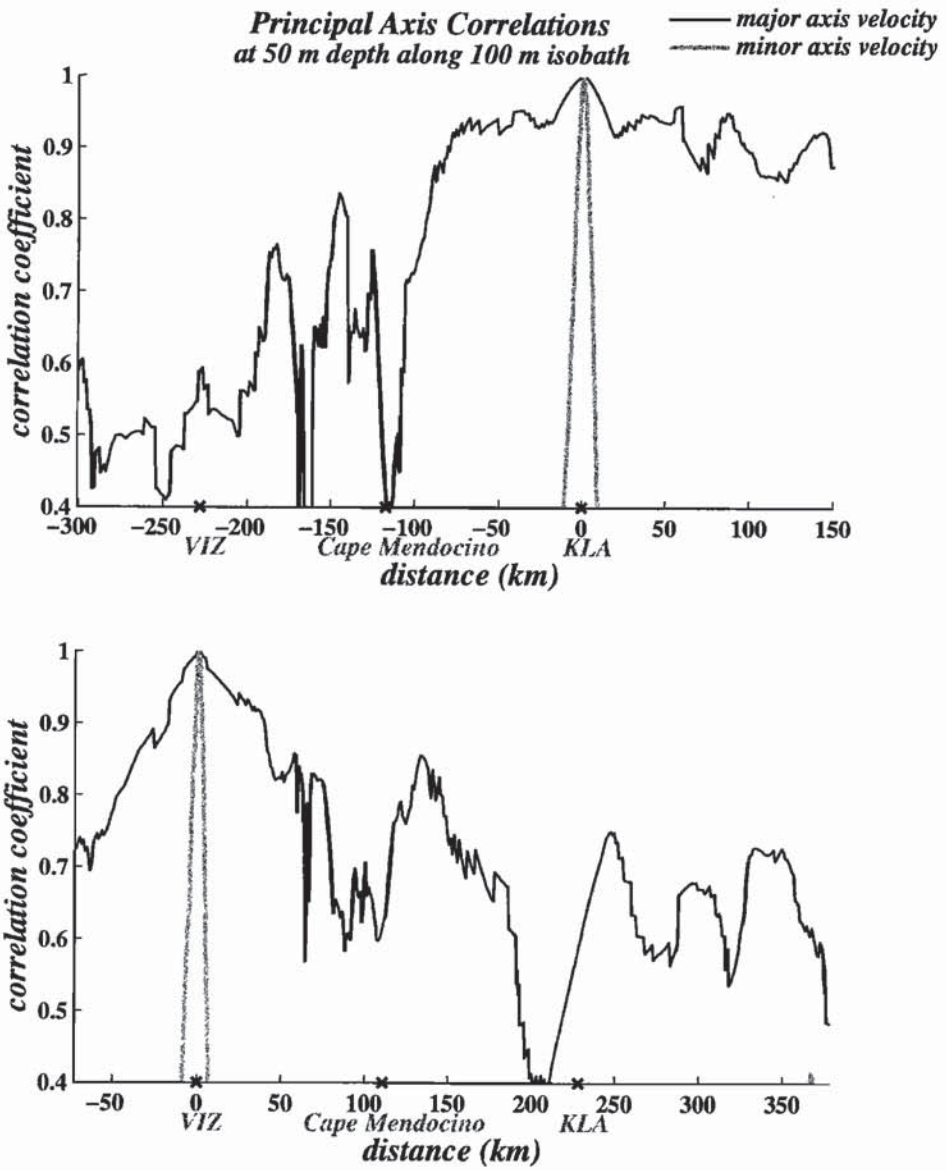

Figure 4. Zero-lagged correlation coefficients for principal axis velocity following the 100 m isobath at 50 m depth. The correlations are relative to the velocity at (top) KLA and (bottom) VIZ.

KLA. Model variability is stronger at all locations than during the NCCCS observational period.

Time-mean surface velocity and rms amplitude of surface velocity for the 100 day simulation with and without rivers (Plate 2) indicate that the buoyancy forcing from the Eel and Klamath Rivers enhances the fluctuations in the surface current over the shelf. The effect of river runoff contributes up to 12 cm s^{-1} to the surface velocity variability over the shelf. This contribution is not distributed uniformly alongshore. Patches of large fluctuations occuring without river runoff north of Point St. George and between the Eel River and Trinidad Head are augmented when river runoff is included. This enhancement of flow variability due to buoyancy forcing is confined to the areas north of Cape Mendocino and is superimposed on the alongshore asymmetry in the current fluctuations that exists between the region north and south of Cape Mendocino in the absence of river runoff.

Mean surface velocity diverges at Cape Mendocino and flows poleward to the north of the cape and equatorward to the south. This divergence pattern with equatorward flow south of Cape Mendocino also occurs in the PWC model mean surface velocity field and may be associated with the large-scale negative wind stress curl south of Cape Mendocino (Plate 1).

Depth-averaged time mean velocities (Plate 3) are muted over the shelf, and their direction along the coast is more variable than was the surface velocity time mean. The asymmetry in variability between regions

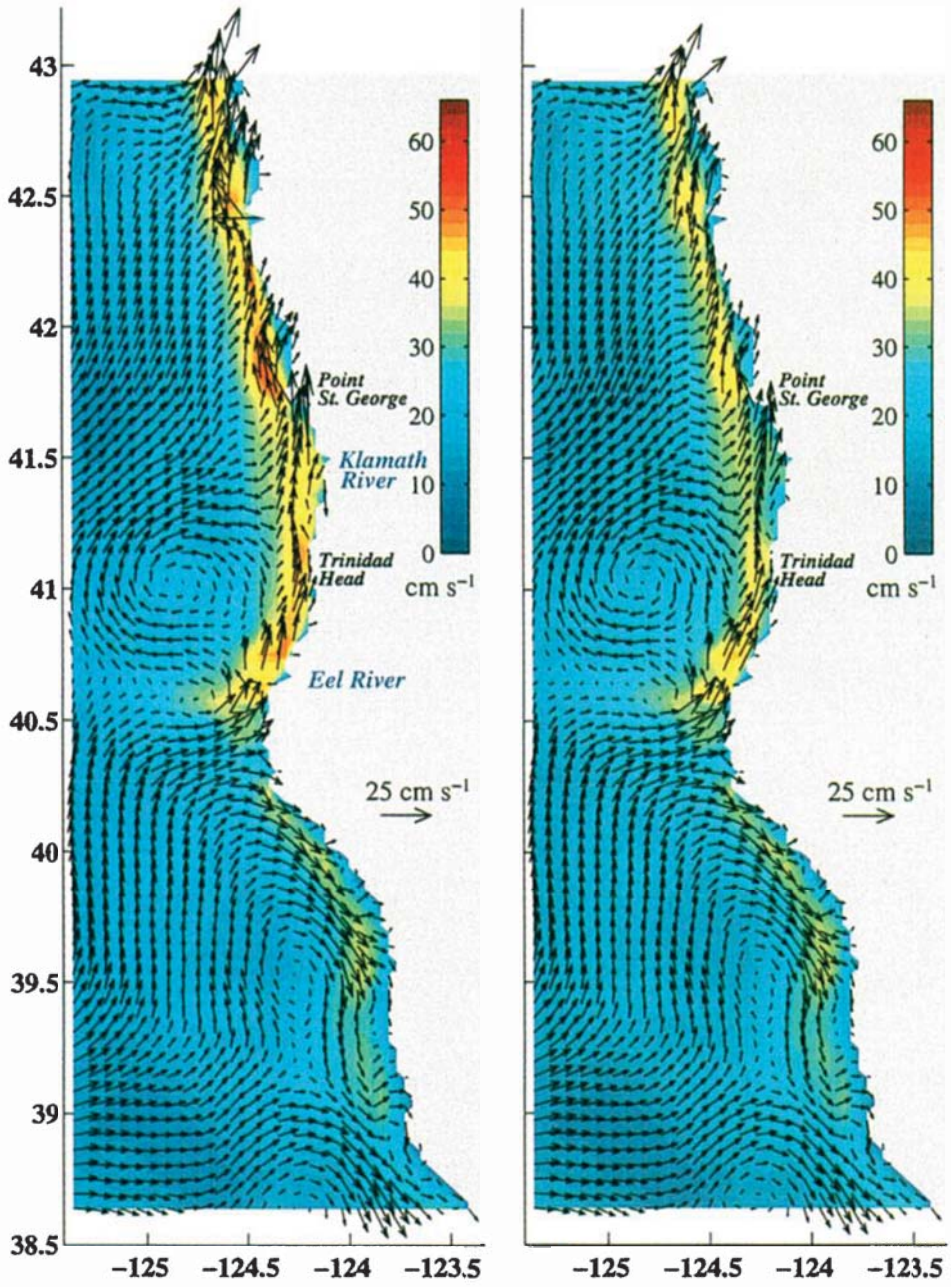

Plate 2. Nested model surface velocity vector mean and rms vector amplitude over the 100 day simulation, (left) with rivers and (right) without rivers. Means are denoted with arrows, while rms amplitude is color contoured. Every second vector is shown in the alongshore and across-shore direction.

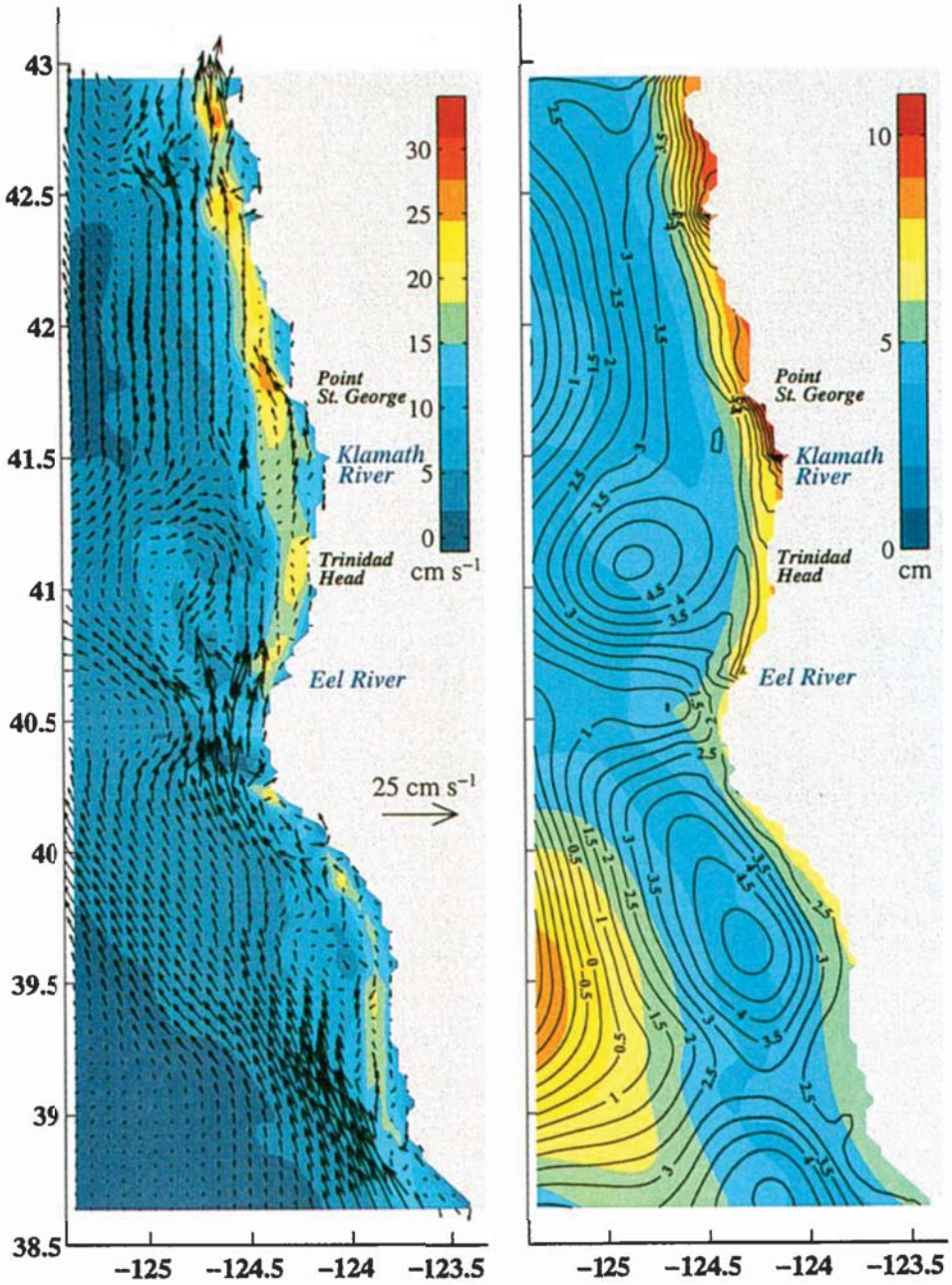

Plate 3. Nested model (left) depth-averaged velocity vector mean and rms vector amplitude over the 100 day simulation with rivers. (Means are denoted with arrows; rms amplitude is color contoured. Every second vector is shown in the along-shore and across-shore direction.) Also shown are (right) surface elevation mean (black contours) and standard deviation (color contours) over the 100 day simulation with rivers.

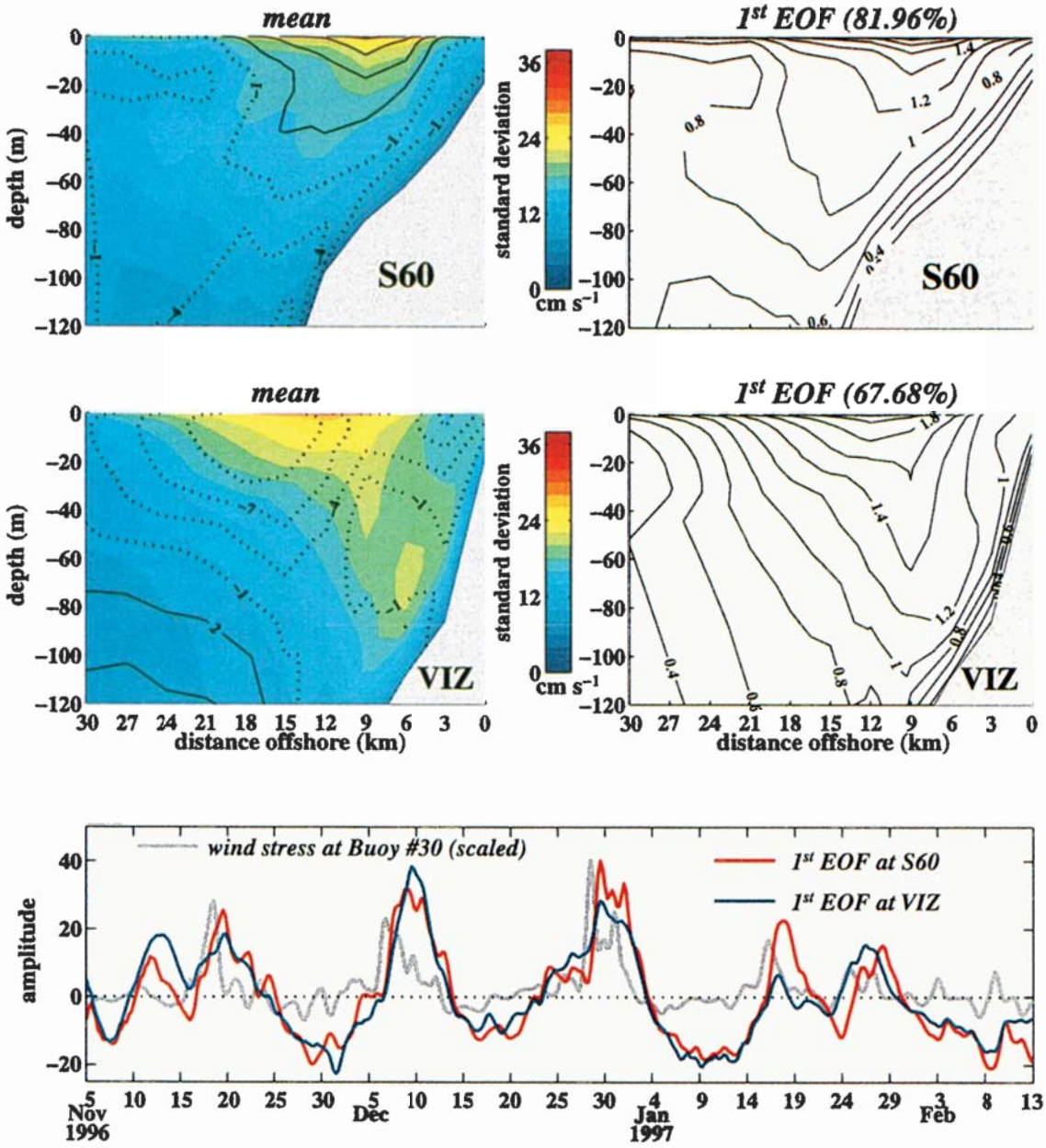

Plate 4. Model mean (contour lines), standard deviation (color shading), and mode 1 EOF of north-south velocity at transects (top) S60 and (middle) VIZ for the nested simulation without rivers. The contour interval for the mean north-south velocity is 3 cm s^{-1}. The percentage of variance explained by the mode 1 EOF is indicated. The amplitude time series of the mode 1 EOF of velocity is shown at the bottom. Wind stress at Cape Mendocino (buoy 30) is included for comparison.

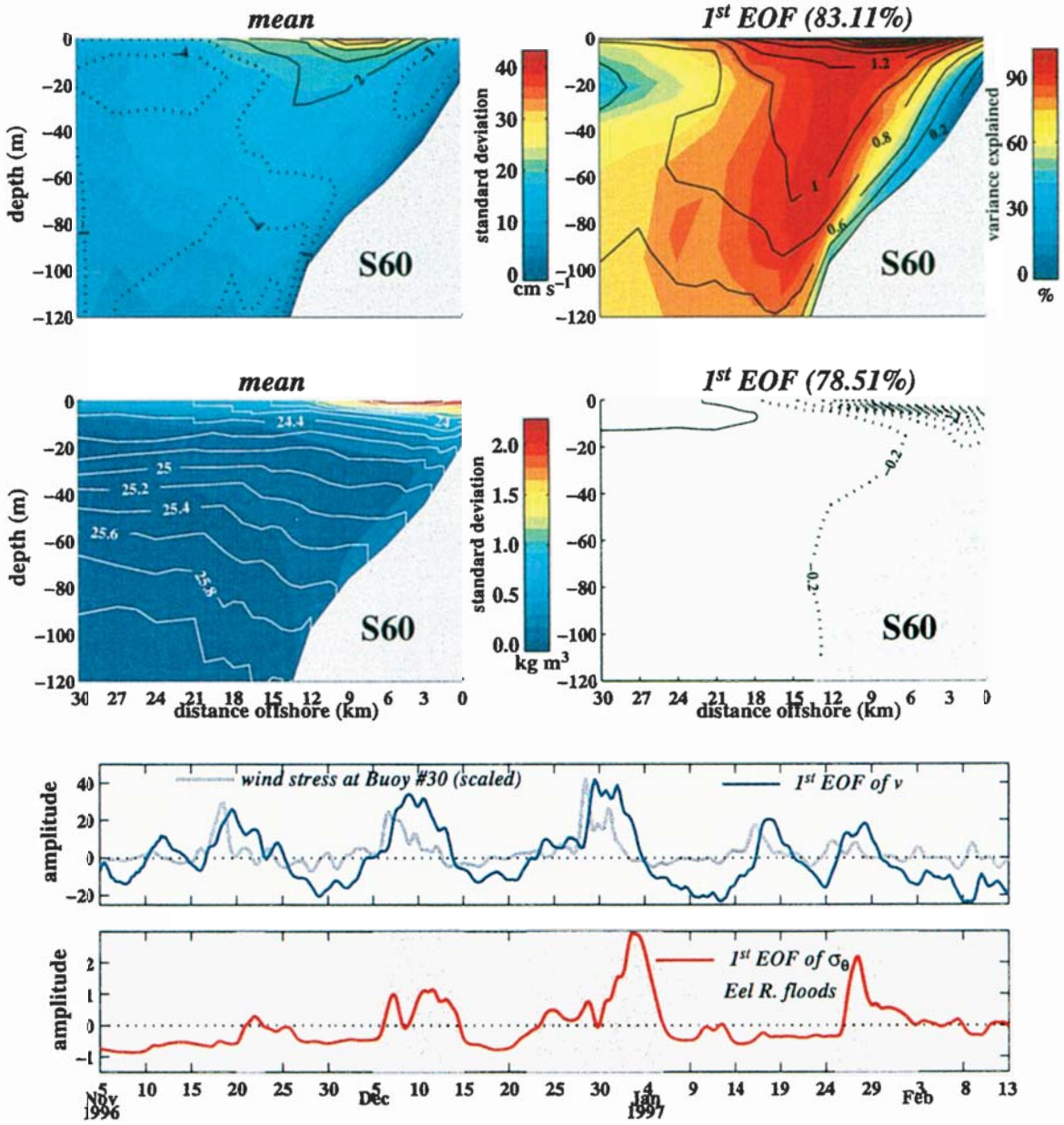

Plate 5. As in Plate 4 but at S60 for the simulation with rivers: (top) North-south velocity v; (middle) potential density σ_θ. In addition, the local percent variance explained by the mode 1 EOF is contoured in color for v. Corresponding amplitude time series for the two variables are shown below.

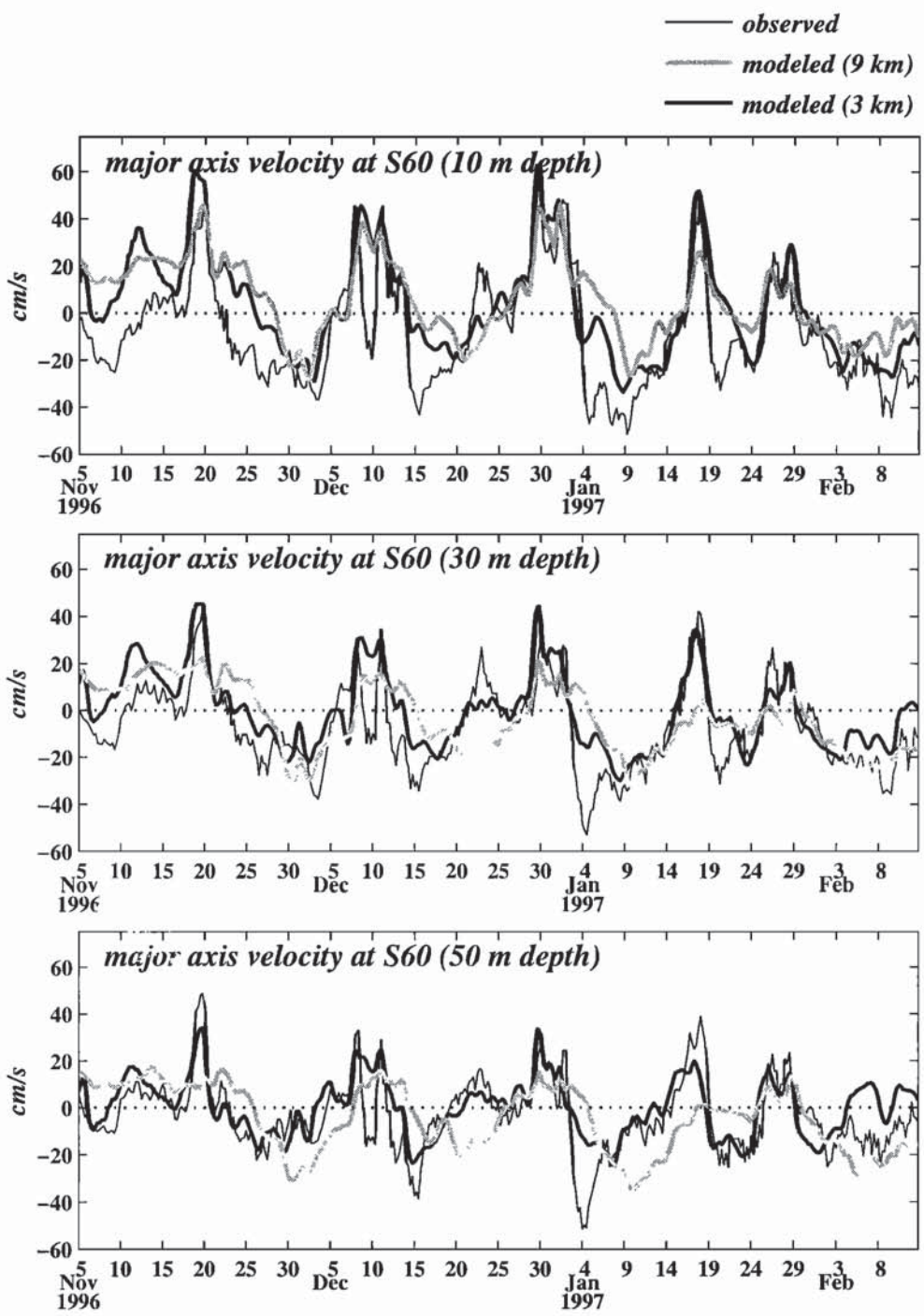

Figure 5. Modeled and observed major axis velocity at the S60 ADCP location on the shelf at three depths over the 100 day record. Velocities are rotated into the principal axes of the depth-averaged current. Observations are shown here courtesy of A. Ogston.

north and south of Cape Mendocino and the enhancement of variability in the same two areas described above are readily apparent. Here, however, there is no discernible difference between variability in the flow with and without rivers (not shown). Mean surface elevation (Plate 3) suggests anticyclonic circulation to the north and south of Cape Mendocino. Variability of sea surface elevation is greatest north of Trinidad Head.

The differences in flow variability north and south of Cape Mendocino, as well as differences due to river runoff, can be further assessed by an examination of model transects of time means, standard deviations, and covariance-based empirical orthogonal functions along east-west (across-shore) sections at VIZ and S60 (Plates 4, 5, and 6). The plots involving alongshore velocity in Plate 4 highlight similarities and differences

Table 3. Observed and Modeled Major Axis Velocity Time Series Statistics at STRATAFORM S60 ADCP Site[a]

	Correlation Coefficient	Mean, cm s^{-1}	Standard Deviation, cm s^{-1}
Observed 10 m		-8.31	22.12
Modeled (3 km) 10 m	0.81	3.09	21.45
Modeled (9 km) 10 m	0.68	5.83	16.49
Observed 30 m		-7.34	17.91
Modeled (3 km) 30 m	0.80	-0.25	16.15
Modeled (9 km) 30 m	0.49	-3.36	14.22
Observed 50 m		-3.27	15.50
Modeled (3 km) 50 m	0.72	0.28	12.30
Modeled (9 km) 50 m	0.32	-4.35	13.85

[a]Observed data courtesy of A. Ogston.

Table 4. Observed and Modeled Minor Axis Velocity Time Series Statistics at STRATAFORM S60 ADCP Site[a]

	Correlation Coefficient	Mean, cm s^{-1}	Standard Deviation, cm s^{-1}
Observed 10 m		-0.05	5.93
Modeled (3 km) 10 m	0.06	0.79	4.12
Modeled (9 km) 10 m	-0.08	1.16	5.79
Observed 30 m		1.97	4.19
Modeled (3 km) 30 m	0.09	0.76	2.31
Modeled (9 km) 30 m	0.15	-0.62	4.26
Observed 50 m		0.21	4.12
Modeled (3 km) 50 m	0.31	0.03	1.76
Modeled (9 km) 50 m	0.06	0.30	3.43

[a]Observed data courtesy of A. Ogston.

north and south of Cape Mendocino and are calculated from the 100 day simulation without rivers. A poleward jet over the midshelf dominates the mean at S60; elsewhere, the flow is equatorward. At the VIZ section the mean velocity is equatorward. On the basis of a comparison of the structure and amplitude of the EOFs, fluctuations in the velocity display a similar pattern at the two transects. The majority of the variance is associated with coastal jet-like motions, concentrated in the upper 40 m, of northward fluctuations during poleward

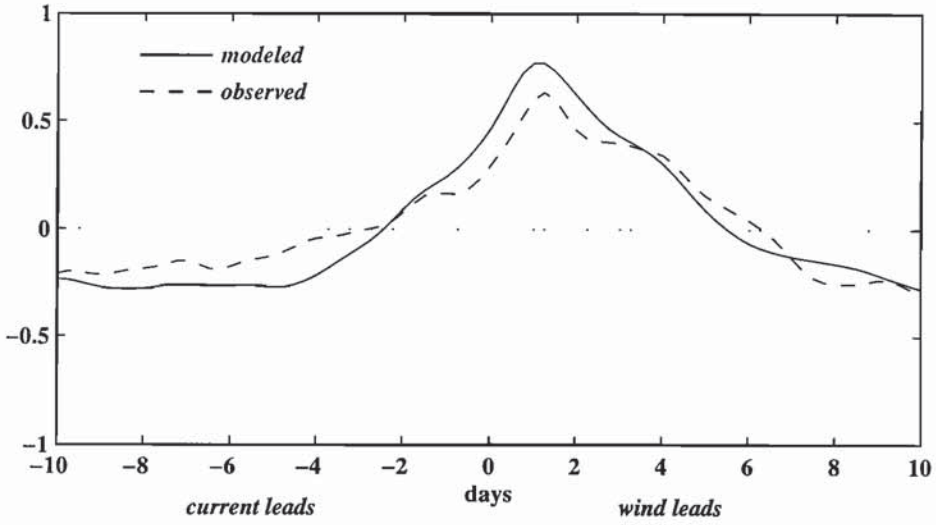

Figure 6. Modeled and observed time-lagged cross correlations of buoy 30 major axis wind stress with major axis 10 m velocity at the S60 ADCP location on the shelf over the 100 day record. NOGAPS model wind stresses are used for the correlation with the nested model. Velocities are rotated into the principal axes of the depth-averaged current.

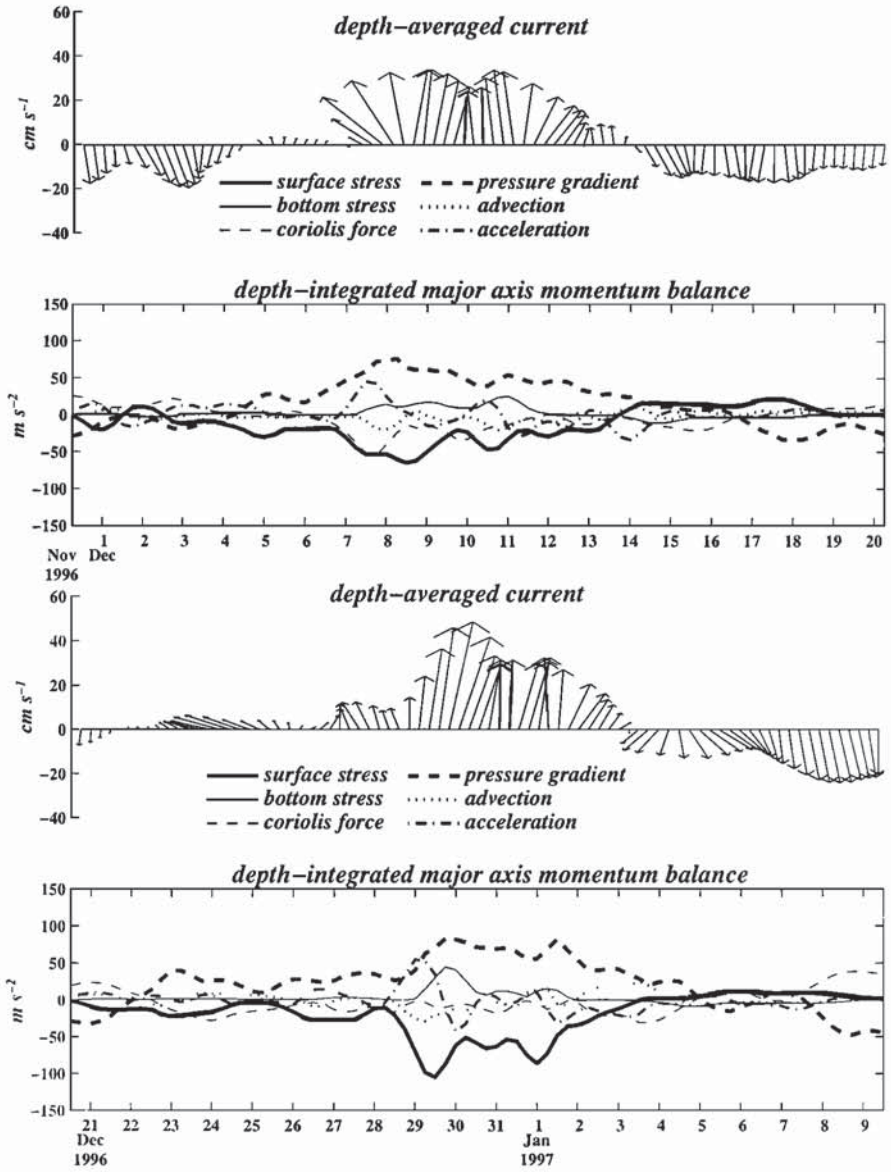

Figure 7. Nested model depth-averaged current and depth-integrated major axis (alongshore) momentum balance at S60 during two storm events. The terms in momentum equation (1) have been divided by the depth D and multiplied by 10^7.

winds and southward fluctuations during equatorwind winds. This is consistent with idealized shelf model response to upwelling and downwelling favorable wind forcing [*Allen and Newberger,* 1996; *Allen et al.,* 1995].

The influence of river discharge on the variability north of Cape Mendocino is documented in Plate 5. Compared to the no river case (Plate 4), mean poleward flow in the jet is slightly stronger when rivers are present. Variability occurs mainly in the upper 5-10 m. This is shallower than the fluctuations that occur without rivers. The mode 1 EOF accounts for a majority of the velocity variance near the surface. This suggests that the effect of the river-induced near-surface stratification is to intensify the wind-driven response in a shallow surface layer. Mean density is distinguished by light Eel River water in the upper 5-10 m. Density fluctuations are concentrated near the surface and occur, as indicated by the EOF amplitude time series, when water lighter than the mean spreads out over the shelf during the Eel River flood events.

To explore the differences in current variability near the surface with and without rivers, we look at the turbulent kinetic energy ($\frac{1}{2}q^2$) from the *Mellor and Yamada* [1982] level 2.5 turbulence submodel along the S60 transect, with and without rivers (Plate 6). Without rivers, turbulent kinetic energy variability is large in the upper 25 m from midshelf to offshore. With rivers, fluctuations in $\frac{1}{2}q^2$ are most intense near the base of

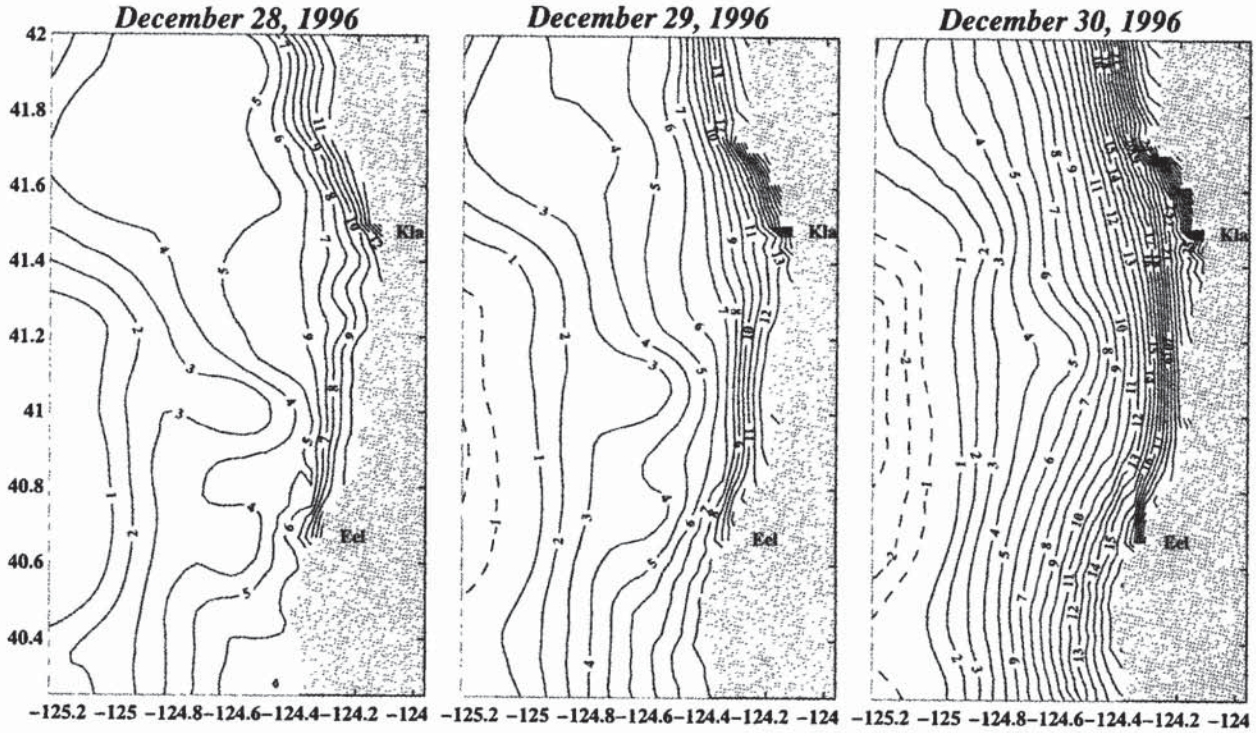

Figure 8. Evolution of sea surface elevation during the early stages of the second severe storm. Units are centimeters.

the strong jet, suggesting the presence of shear-induced turbulence. The $\frac{1}{2}q^2$ amplitude time series tracks wind stress so that turbulent kinetic energy increases during strong wind events. The strong stratification caused by river runoff may confine intense $\frac{1}{2}q^2$ values over the midshelf to within about 10 m of the surface. Though $\frac{1}{2}q^2$ means and standard deviations are larger in this near-surface region for the rivers case compared with the no rivers case, nonetheless, over midshelf the no rivers case has large $\frac{1}{2}q^2$ values that extend more deeply vertically by about 15 m than those of the rivers case.

We have assessed the structure of means, standard deviations, and dominant EOFs at isolated transects. To conclude this section, we evaluate the degree of communication between regions north and south of Cape Mendocino. Figure 4 shows the alongshore space-lagged velocity correlation coefficients relative to velocity at KLA and VIZ at 50 m depth over the 100 m isobath. At each location along the coast the velocity is rotated into the principal axes of the depth-averaged velocity. Correlation coefficients are calculated for both the major and minor axes components. Minor axis correlation scales are on the order of 10 km. Short alongshore correlation scales of the across-shore (minor axis) velocity components, in contrast to the relatively long alongshore correlation scales of the alongshore (major axis) velocity components along the coast, are typical features of coastal flow regimes off the northern U.S. west coast [*Kundu and Allen,* 1976; *Dever,* 1997b]. Major axis correlation lengths extend around Cape Mendocino. However, the magnitude of the correlations falls rounding Cape Mendocino. For the correlations anchored at KLA, magnitudes are lower to the south of Cape Mendocino but remain high to the north. For the correlations anchored at VIZ, magnitudes drop off to the north and south.

5. Time Series

Modeled and observed major axis velocity time series at three depths at the S60 ADCP site (40.89°N, 124.25°W) are compared in Figure 5. The S60 ADCP (RDI workhorse) observations are described by *Ogston et al.* [2000]. The correlation coefficients are considerably higher for the nested high-resolution model (3 km) relative to those of the PWC model (9 km) (Table 3). Correlations remain high for the nested model throughout the water column, whereas correlations drop off sharply with depth for the PWC model. Observed time mean flow is equatorward at all depths. Neither model reproduces the mean flow. The second nested model (1 km), however, does reproduce the observed time mean vertical current structure [*Pullen and Allen,* 2000]. Observed standard deviations are higher near the surface and lower near the bottom. The magnitudes of the standard deviations from the nested model are in reasonable qualitative agreement with the observed values and replicate the reduction

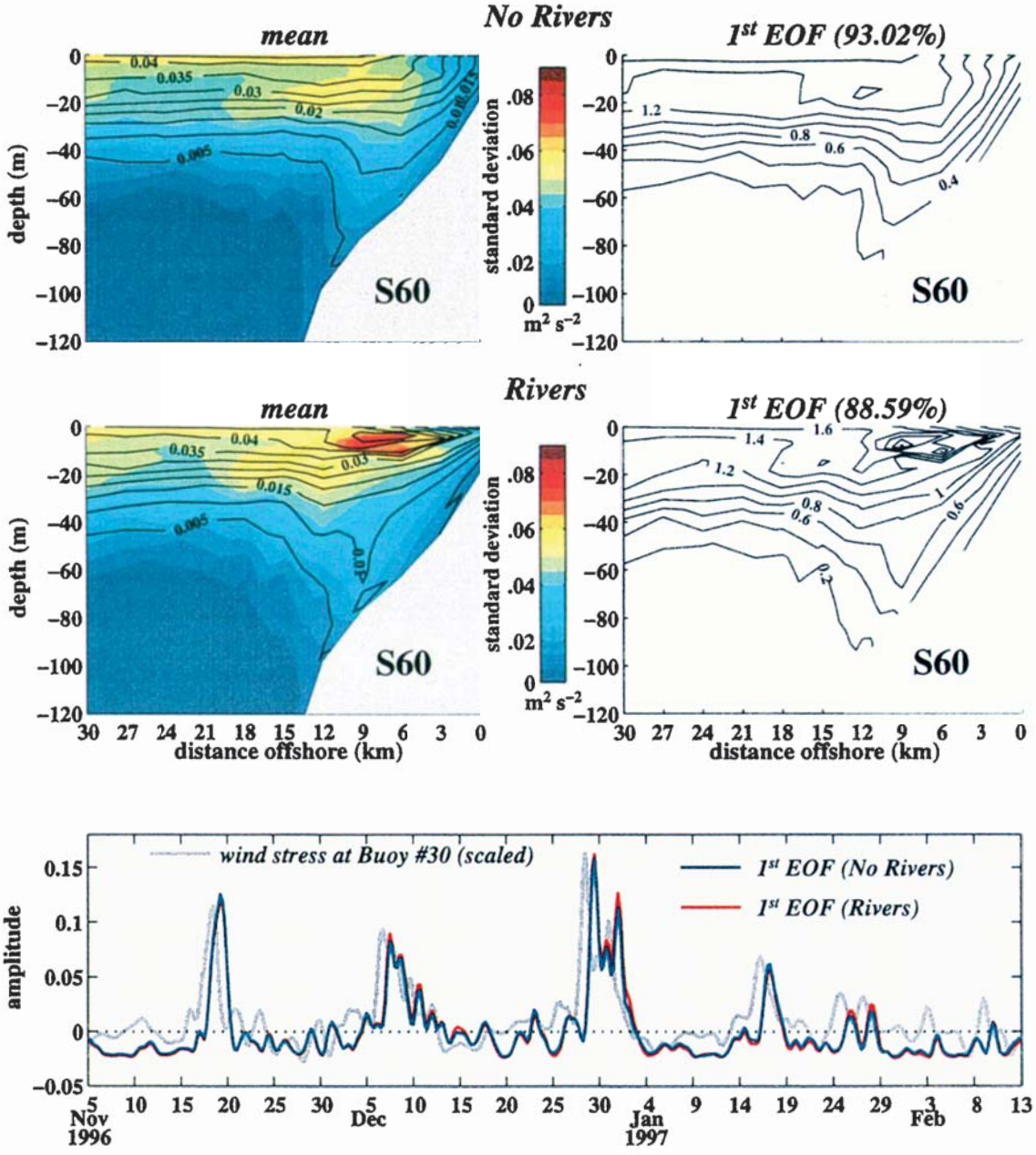

Plate 6. As in Plate 4 but for turbulent kinetic energy $\frac{1}{2}q^2$ at S60 with and without river... Turbulent kinetic energy has been multiplied by 10^2.

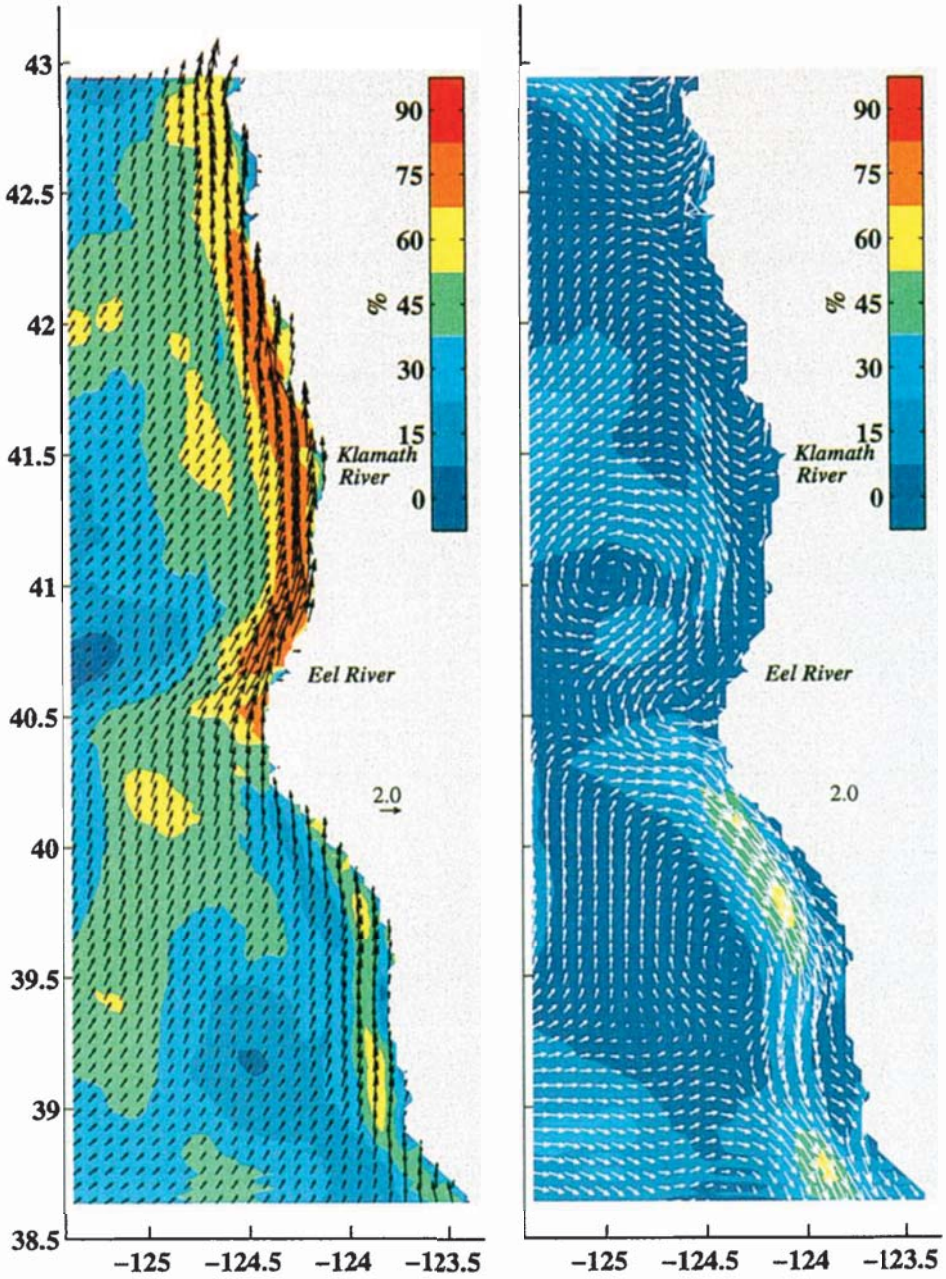

Plate 7. Map of dominant surface velocity mean product EOFs (arrows). (left) Modes 1 and (right) 2 are shown. Percent mean product explained is 58.34% and 13.81%, respectively. Color contours show the amount of total mean product at each site explained by the mode. The simulation with rivers is used.

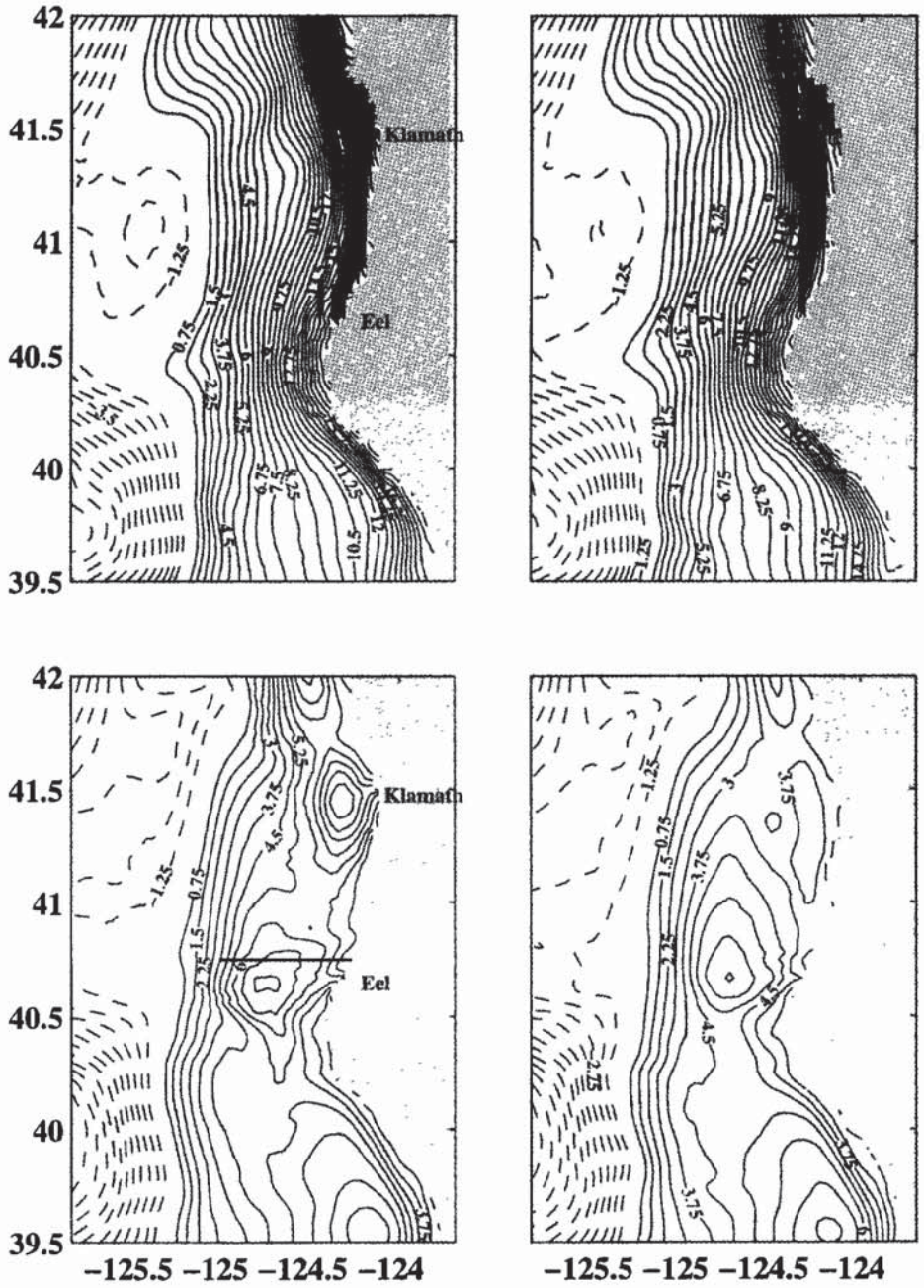

Figure 9. Sea surface elevation on (top) December 31, 1996, and (bottom) January 6, 1997, during the second major storm, (left) with rivers and (right) without rivers. Units are centimeters. The east-west line at 40.75°N marked on the bottom left panel is the location of the east-west sections plotted in Figure 12.

with depth. The PWC model has standard deviations that are smaller in magnitude at 30 m and above and are more uniform with depth. The magnitude of both the observed and modeled minor axes mean values are small (<2 cm s^{-1})(Table 4). Standard deviations are <6 cm s^{-1} and they decrease with depth in the model and in the observed data. The largest correlation with observed values occurs for the nested model at 50 m depth.

Modeled and observed major axis wind-current time-lagged cross-correlations illustrate the nested model's skill at reproducing the observed wind-forced response (Figure 6). The maximum wind-current cross-correlation value of the model (observations) of 0.77 (0.63) occurs at 1 day (1.25 days).

The depth-averaged current at the S60 site along with terms in the nested model depth-integrated alongshore momentum balance [*Blumberg and Mellor*, 1987]

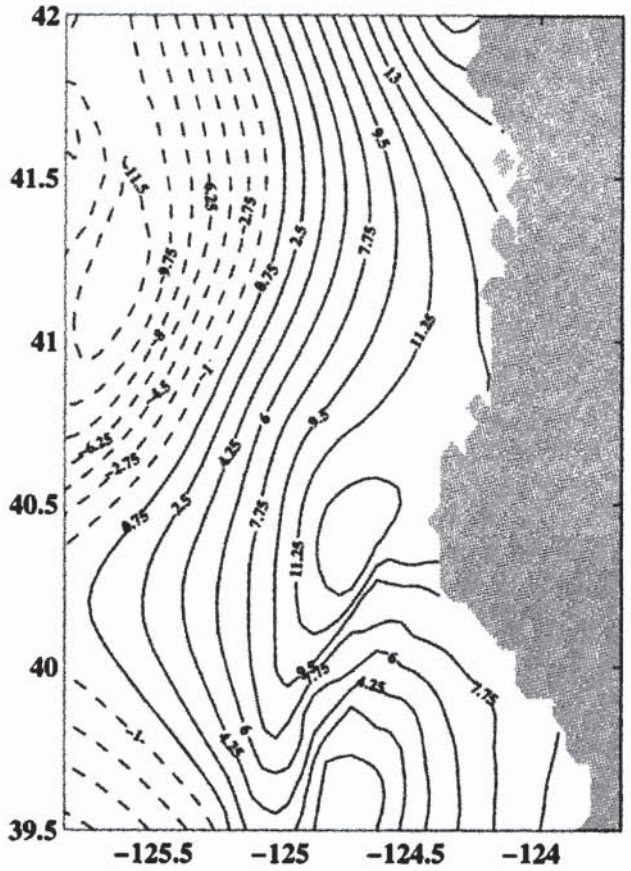

Figure 10. TOPEX/ERS-2 altimeter snapshot of height field anomalies on January 6, 1997. Units are centimeters. Processing of satellite data was done by C. James.

$$\underbrace{\frac{\partial VD}{\partial t}}_{(1)} + \underbrace{\frac{\partial UVD}{\partial x} + \frac{\partial V^2 D}{\partial y}}_{(2)} - F_y - G_y + \underbrace{fUD}_{(3)} - \underbrace{\frac{\tau_{ys}}{\rho_0}}_{(4)} + \underbrace{\frac{\tau_{yb}}{\rho_0}}_{(5)} + \underbrace{gD\frac{\partial \eta}{\partial y} + \frac{gD}{\rho_0}\int_{-1}^{0}\int_{\sigma}^{0}\left(D\frac{\partial \rho'}{\partial y} - \frac{\partial D}{\partial y}\sigma'\frac{\partial \rho'}{\partial \sigma}\right)d\sigma' d\sigma}_{(6)} = 0, \quad (1)$$

during the two major storm events are shown in Figure 7. The terms are (1) acceleration, (2) advection (plus horizontal diffusion), (3) Coriolis force, (4) surface stress, (5) bottom stress, and (6) pressure gradient. The alongshore balance above is obtained by rotating the original x (east-west) and y (north-south) equations into the principal axis orientation of the depth-averaged current.

The time-dependent term balance and currents demonstrate a generic response to passing storms. In particular, the surface stress exerted by the winds accelerates a poleward current. Bottom friction increases to retard the accelerating current. Meanwhile, an equatorward pressure gradient develops that primarily balances the wind-forced offshore flow below the surface layer. After the relaxation of the surface stress the wind-forced across-shelf flow decreases so that it is no longer large enough to balance the pressure gradient. As a result, the surviving pressure gradient accelerates the alongshore current southward and leads to current reversals on December 14 and January 3. The major axis depth-averaged currents and the important terms in the momentum balance have larger magnitudes in response to the second (stronger) storm. The minor axis momentum balance is predominantly geostrophic and is not shown.

The development of the southward pressure gradient force is shown in maps of surface elevation (Figure 8). After December 28, as poleward winds grow strong, the surface elevation develops alongshore variations. In particular, the regions south of Trinidad Head (41.1°N), where S60 is situated, and south of Point George (41.7°N) experience a sea level setup that establishes an alongshore pressure gradient.

6. Circulation Patterns

Nested model sea surface elevation during the second major storm is shown in Figure 9 for the simulation with and without rivers. Winds are strongly poleward on December 31. Sea level setup against the coast, emblematic of downwelling, is evident at these times. Alongshore spatial inhomogeneities in sea level elevation are present because of both coastline irregularity and rivers. River runoff creates a buoyancy current that augments the sea level setup and enhances the coastal downwelling jet [*Fong*, 1998].

On January 6, wind stress reverses to equatorward and sea level elevation domes to form an anticyclonic eddy centered near 40.75°N. The strength of the elevation "high" is increased by river runoff, but the eddy is present even without river runoff. By contrast, the high sea level cell adjacent to the Klamath River is absent when river runoff is not included. The same pattern of eddy occurrence with and without rivers appears during the first storm of December 8–17; however, the magnitude of sea level elevation is reduced.

Fortuitously, an ERS-2 satellite track crossed the waters near Cape Mendocino on January 6. TOPEX/ERS-2 satellite altimetry confirms the presence of a clockwise (anticyclonic) eddy adjacent to Cape Mendocino (Figure 10) on January 6. The broad poleward flow offshore of the remotely sensed eddy is also found in the model simulation. Furthermore, the anticyclonic circulation south of Cape Mendocino in the satellite field is also indicated in the model sea surface height field.

The evolution of the eddy near the end of the second storm is traced in maps of depth-averaged veloc-

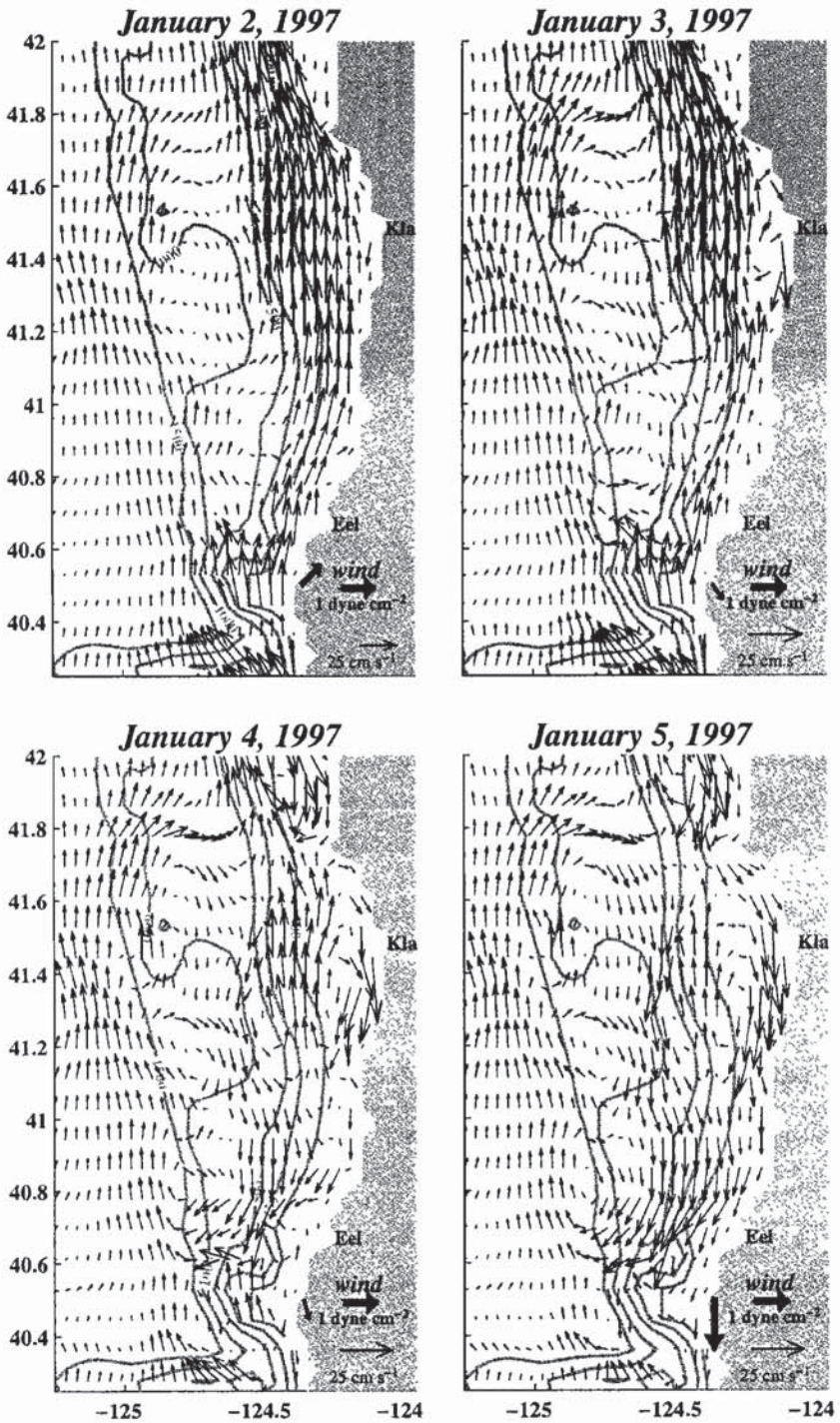

Figure 11. Maps of depth-averaged velocity north of Cape Mendocino. Wind stress at buoy 30 is indicated with a thick arrow. The eddy formation adjacent to the Eel and Klamath Rivers is shown.

ity (Figure 11). The reversal of the coastal current from poleward (January 2) to equatorward (January 5) is accompanied by a complicated pattern of eddies and meanders. Notably, the eddies adjacent to the Eel and Klamath Rivers start to form January 3. From the behavior of the depth-averaged velocity vectors in the vicinity of the Eel River it appears that the shelf and slope bottom topographic variations associated with the Eel River canyon just south of about 40.6°N play a major role in the formation of the eddy in this region.

An east-west section of velocity cutting through the eddy (see Figure 9 for location of the section) extending about 60 km offshore shows the depth structure of the eddy (Figure 12). The eddy reaches deeper than 500 m

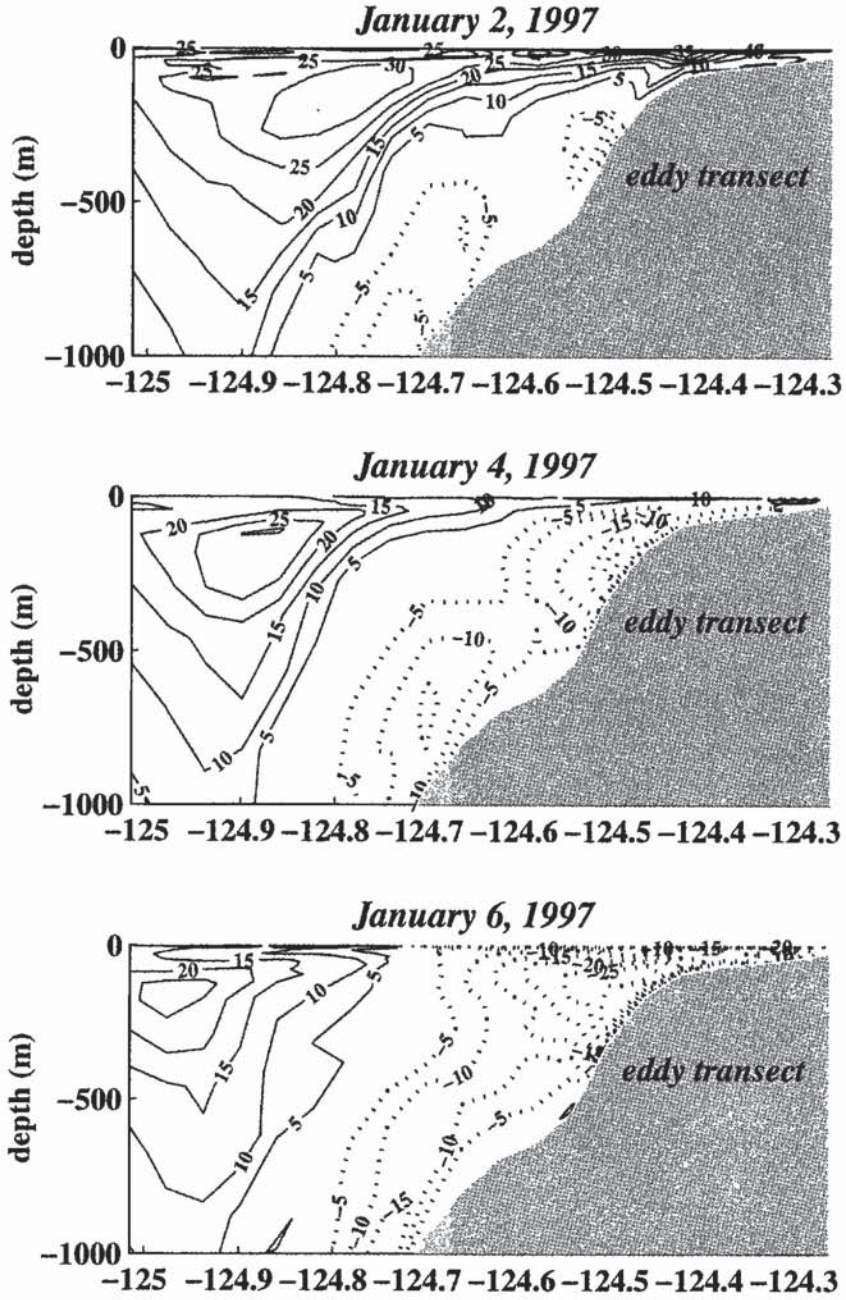

Figure 12. East-west section at 40.75°N of north-south velocity through the eddy pictured in Figure 9. Units are cm s^{-1}. The model simulation with rivers is shown. The sections extend ~60 km offshore.

and has a subsurface maximum of 25 cm s^{-1} at about 100 m depth. The equatorward limb of the eddy forms over the shelf by January 6. At later times the eddy moves offshore and decays as upwelling favorable winds influence the region (not shown). The eddy has a similar depth structure during the first storm, though the velocities are about 5-10 cm s^{-1} weaker.

The eddy circulation associated with the Klamath River to the north has very different characteristics. That eddy occurs only when rivers are present in the simulation and is situated over the shelf. Velocities in that eddy are surface-intensified during both storms.

The signature of the eddy near the Eel River comes through in the mean depth-averaged current (Plate 3), as well as in the mean surface velocity (Plate 2). Maps of the first and second mean product EOFs of surface currents calculated with the mean values retained (Plate 7) and corresponding amplitude time series (Figure 13) identify the eddy as part of a mode 2 (explaining ~14% of the mean product) response to the relaxations/reversals of poleward winds. This second mode is characterized during the wind relaxation by mostly equatorward flow over the shelf. In this mode an anticyclonic eddy is also found to the south, in the fold

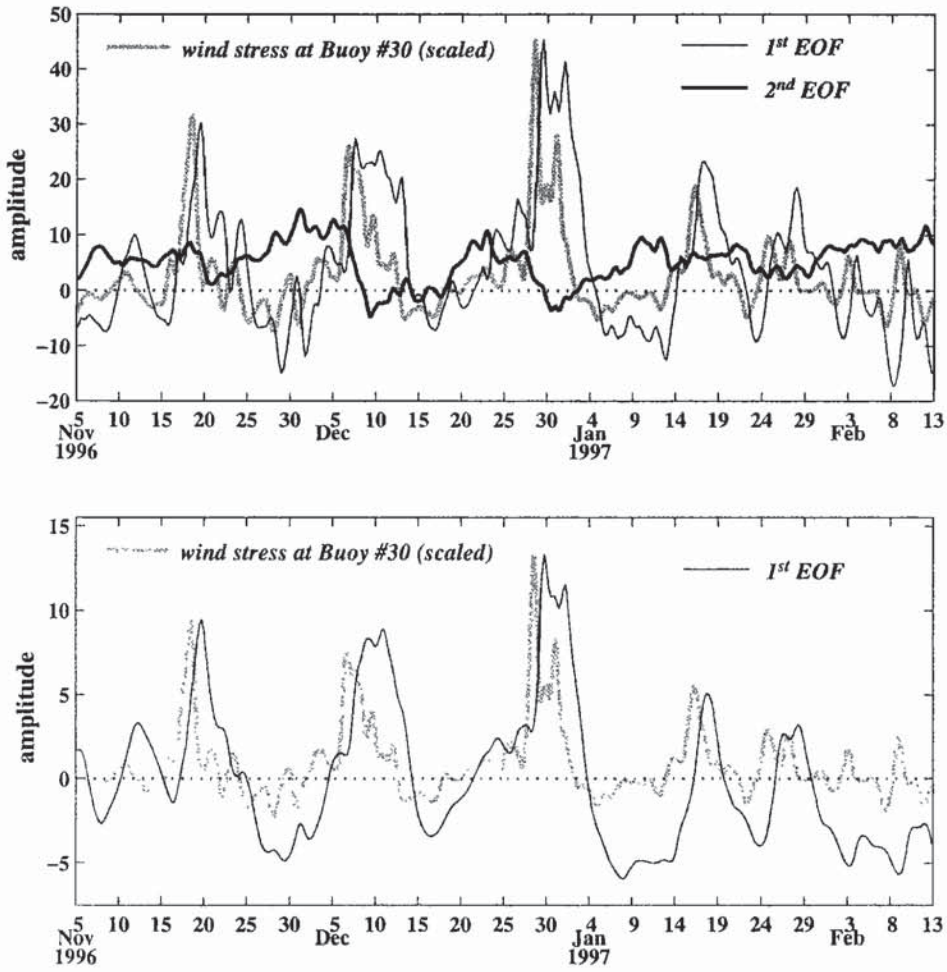

Figure 13. (top) Amplitude time series for modes 1 and 2 of the mean product EOFs of surface velocity shown in Plate 7 and (bottom) amplitude time series for mode 1 of the EOF of depth-averaged velocity shown in Plate 8. NOGAPS major axis wind stress at Cape Mendocino (buoy 30) is also shown.

of Cape Mendocino. The relatively large amplitudes and large fraction of local mean product explained in the near-coastal surface currents south of Cape Mendocino indicate that this mode, whose variability is separate from that of the mode 1 large scale wind-forced response, makes a dominant contribution to the mean southward currents south of Cape Mendocino (Plate 2). The first mode EOF (explaining about 58% of the mean product) represents a coastal current that has a larger magnitude and represents a larger fraction of the local mean product north of Cape Mendocino. The variability of the first mode is clearly related to that of the wind stress (Figure 13). The maximum time-lagged correlation coefficient is 0.89 at a lag of 24 hours. This mode represents a large alongshore-scale coastal circulation response to wind forcing with greatest strength north of Cape Mendocino. The portion of the surface velocity mean product attributable to the other modes drops off sharply; mode 3 contributes 7%. Thus two modes explain the majority of the surface velocity mean product and characterize the coherent coastal surface current response to storm events.

The depth-averaged velocity mode 1 EOF (Plate 8), calculated as is usual with the mean values removed, represents a large-scale coastal current fluctuation that is strongest north of Cape Mendocino but that is also appreciable both in relative amplitude and in fraction of local variance represented, south of Cape Mendocino. The amplitude time series of this mode is highly correlated with the wind stress ($r = 0.85$) at a lag of 36 hours. Thus this mode represents a large-scale coherent coastal current response to wind that extends from about 39°N to north of 43°N. The extension of this coherent wind-driven response south of Cape Mendocino was masked in the surface current mean product EOFs in Plate 7 by the unrelated variability of the mode 2 coastal surface currents south of Cape Mendocino.

7. Discussion and Summary

We have conducted the first high-resolution numerical study of winter circulation around Cape Mendocino. We have examined the contributions of major forcing mechanisms to the circulation in the region using a sta-

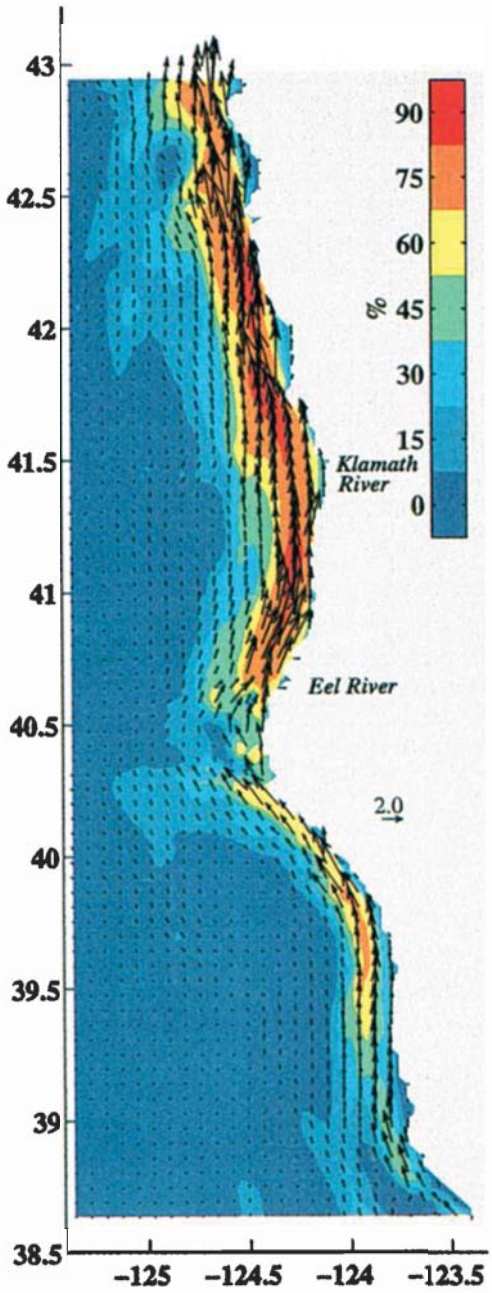

Plate 8. Map of mode 1 depth-averaged velocity EOF (arrows). Percent variance explained is 56.57%. Color contours show the amount of total variance at each site explained by the mode. The simulation with rivers is used.

tistical approach. In the absence of river forcing the asymmetry in flow variability north and south of Cape Mendocino, with the flow exhibiting more energetic behavior to the north, is likely related to the alongshore variations in wind forcing.

Primarily associated with the flood events, river discharge bathes the near-surface (upper 5–10 m) waters of the shelf, with light water enhancing the stratification near the surface. The buoyancy input serves to amplify the wind-driven response in a thin surface layer and increases the magnitude of velocity fluctuations in the coastal jet.

Major and minor axes 50 m alongshore velocity correlations along the 100 m isobath were computed at points north and south of Cape Mendocino. Minor axis (across-shore) correlation scales are about 10 km. Major axis (alongshore) correlation scales are >100 km over the broad shelf region to the north of Cape Mendocino and shorter on the narrower shelf to the south of Cape Mendocino. Alongshore velocity correlations are reduced to the south of Cape Mendocino.

Good agreement is found between the amplitude and time variability of the nested model major axis currents and the observed ADCP major axis currents at three depths at the S60 location during the 100 day simulation. The nested model (3 km) performed better than the PWC (9 km) model, especially at deeper depths. At the shelf site, terms in the depth-integrated major axis momentum balance displayed a common time evolution to passing storms. This response includes the establishment of an alongshore pressure gradient force that helps initiate and sustain a current reversal over the shelf. The current reversal at the shelf site develops into the shoreward arm of an anticyclonic eddy. The eddy occurrence was verified by satellite altimetry. In addition, the eddy was described as a local generic response to traveling atmospheric cyclones through an EOF analysis of velocity. The interaction of the Eel River plume with the eddy and the implications of eddy circulation for sediment transport on the shelf are addressed by *Pullen and Allen* [2000].

Appendix A: River Input

River runoff from the Eel and Klamath Rivers is discharged into all three model domains using the method described by *Kourafalou et al.* [1996]. The modifications to the governing equations at the location of the river input are reviewed here.

The vertically integrated continuity equation becomes

$$\frac{\partial \eta}{\partial t} + \frac{\partial \bar{U} D}{\partial x} + \frac{\partial \bar{V} D}{\partial y} = \bar{q}.$$

Here $\bar{q} = Q/\Delta x \Delta y$, where Q is the river discharge (in $m^3\ s^{-1}$) and Δx and Δy are the horizontal grid spacing.

The three-dimensional continuity equation becomes

$$\frac{\partial \eta}{\partial t} + \frac{\partial \omega}{\partial \sigma} + \frac{\partial UD}{\partial x} + \frac{\partial VD}{\partial y} = q'(k),$$

where $q'(k)$ must satisfy the constraint

$$\sum_{k=1}^{K} q'(k)\Delta\sigma(k) = \bar{q}.$$

Here k is an index for the vertical σ level, K is the number of σ levels, and $\Delta\sigma(k)$ is the spacing between

adjacent σ levels: $\sigma(k) - \sigma(k+1)$. Let $P(k)$ be the fraction of discharge, $\bar{q}$, put in at σ level k. Then we find the value of $q'(k)$ by

$$q'(k) = \frac{P(k)\bar{q}}{\Delta\sigma(k)},$$

where

$$\sum_{k=1}^{K} P(k) = 1.$$

If the river is input uniformly with depth, then $P(k) = \Delta\sigma(k)$. Whereas if the river is input only in the top layer, as first described and implemented by *Kourafalou et al.* [1996] and used in this paper, then $P(1) = 1$ and $P(k) = 0$ for $k \neq 1$.

The salinity equation becomes

$$\frac{\partial SD}{\partial t} + \frac{\partial SUD}{\partial x} + \frac{\partial SVD}{\partial y} + \frac{\partial S\omega}{\partial \sigma} =$$

$$q'(k)S_{\text{river}} + \frac{\partial}{\partial \sigma}\left[\frac{K_H}{D}\frac{\partial S}{\partial \sigma}\right] + F_S,$$

while the temperature equation becomes

$$\frac{\partial TD}{\partial t} + \frac{\partial TUD}{\partial x} + \frac{\partial TVD}{\partial y} + \frac{\partial T\omega}{\partial \sigma} =$$

$$q'(k)T_{\text{river}} + \frac{\partial}{\partial \sigma}\left[\frac{K_H}{D}\frac{\partial T}{\partial \sigma}\right] + F_T,$$

where S_{river} and T_{river} are the salinity and temperature, respectively, of the river discharge. In the application described in this paper, $S_{\text{river}} = 0$ and $T_{\text{river}} = 11.5°\text{C}$ on all model domains. In the first nested model the river discharge is put into the top layer at the innermost grid cell of a two grid cell long inlet channel of one grid cell width.

Acknowledgments. We thank Corinne James for discovering the eddy in satellite altimetry and for contributing the satellite data in Figure 10. The assistance of Priscilla Newberger in model implementation is gratefully acknowledged. This work was supported in part by a grant of Cray C90, T90, and SV1 time from the Department of Defense Major Shared Resource Centers at Wright-Patterson Air Force Base and at the Naval Oceanographic Office. This work was funded by the Office of Naval Research through grants N00014-93-1-0804, N00014-93-1-1301, and N00014-97-1-0165.

References

Allen, J. S., and P. A. Newberger, Downwelling circulation on the Oregon continental shelf, part I, Response to idealized forcing, *J. Phys. Oceanogr., 26,* 2011-2035, 1996.

Allen, J. S., P. A. Newberger, and J. Federiuk, Upwelling circulation on the Oregon continental shelf, part I, Response to idealized forcing, *J. Phys. Oceanogr., 25,* 1843-1866, 1995.

Beardsley, R. C., and S. J. Lentz, The Coastal Ocean Dynamics Experiment collection: An introduction, *J. Geophys. Res., 92,* 1455-1463, 1987.

Blumberg, A. F., and G. L. Mellor, A description of a three-dimensional coastal ocean circulation model, in *Three-Dimensional Coastal Ocean Models, Coastal Estuarine Sci.*, vol. 4, edited by N.S. Heaps, pp. 1-16, AGU, Washington, D.C., 1987.

Clancy, R. M., P. W. deWitt, P. May, and D. S. Ko, Implementation of a coastal ocean circulation model for the west coast of the United States, paper presented at American Meteorological Society Conference on Coastal Oceanic and Atmospheric Prediction, Atlanta, Ga., 1996.

Clark, T. L., and R. D. Farley, Severe downslope windstorm calculations in two and three spatial dimensions using anelastic interactive grid nesting: A possible mechanism for gustiness, *J. Atmos. Sci., 41,* 329-350, 1984.

Dever, E. P., Wind-forced cross-shelf circulation on the northern California shelf, *J. Phys. Oceanogr., 27,* 1566-1580, 1997a.

Dever, E. P., Subtidal velocity correlation scales on the northern California shelf, *J. Geophys. Res., 102,* 8555-8572, 1997b.

EG&G, Inc., Circulation on the Northern California shelf and slope: Final Report of the Northern California Coastal Circulation Study, *Oceanogr. Serv. Rep. NCCCS-91-2,* 371 pp., Washington Anal. Serv. Cent., Waltham, Mass., 1991.

Fong, D. A., Dynamics of freshwater plumes: Observations and numerical modeling of the wind-forced response and alongshore freshwater transport, Ph.D. dissertation, 172 pp., Mass. Inst. of Technol./Woods Hole Oceanogr. Inst. Joint Program, Woods Hole, 1998.

Halliwell, G. R., and J. S. Allen, The large scale coastal wind field along the west coast of North America, 1981-1982, *J. Geophys. Res., 92,* 1861-1884, 1987.

Hogan, T., and T. Rosmond, The description of the Navy Operational Global Atmospheric Prediction System's spectral forecast model, *Mon. Weather Rev., 119,* 1786-1815, 1991.

Kourafalou, V. H., L.-Y. Oey, J. D. Wang, and T. L. Lee, The fate of river discharge on the continental shelf, 1, Modeling the river plume and the inner shelf coastal current, *J. Geophys. Res., 101,* 3415-3434, 1996.

Kundu, P. K., and J. S. Allen, Some three-dimensional characteristics of low-frequency current fluctuations near the Oregon coast, *J. Phys. Oceanogr., 6,* 181-199, 1976.

Large, W. G., and S. Pond, Open ocean momentum flux measurements in moderate to strong winds, *J. Phys. Oceanogr., 11,* 324-336, 1981.

Largier, J. L., B. A. Magnell, and C. D. Winant, Subtidal circulation over the northern California shelf, *J. Geophys. Res., 98,* 18,147-18,179, 1993.

Lentz, S. J., and J. Trowbridge, A dynamical description of fall and winter mean current profiles over the northern California shelf, *J. Phys. Oceanogr., 31,* 914-931, 2001.

Mellor, G. L., and T. Yamada, Development of a turbulence closure model for geophysical fluid problems, *Rev. Geophys., 20,* 851-875, 1982.

Mellor, G. L., T. Ezer, and L.-Y. Oey, The pressure gradient conundrum of sigma coordinate ocean models, *J. Atmos. Oceanic Technol., 11,* 1126-1134, 1994.

Nittrouer, C. A., STRATAFORM: Overview of its design and synthesis of its results, *Mar. Geol., 154,* 3-12, 1999.

Oey, L.-Y., Flow around a coastal bend: A model of the Santa Barbara Channel eddy, *J. Geophys. Res., 101,* 16,667-16,682, 1996.

Ogston, A. S., D. A. Cacchione, R. W. Sternberg, and G. C. Kineke, Observations of storm and river flood-driven

sediment transport on the northern California continental shelf, *Cont. Shelf Res., 20,* 2141-2162, 2000.

Pullen, J. D., Modeling studies of the coastal circulation off northern California, Ph.D. dissertation, 145 pp., Oregon State Univ., Corvallis, 2000.

Pullen, J. D., and J. S. Allen, Modeling studies of the coastal circulation off northern California: Shelf response to a major Eel River flood event, *Cont. Shelf Res., 20,* 2213-2238, 2000.

Strub, P. T., J. S. Allen, A. Huyer, and R. L. Smith, Seasonal cycles of currents, temperatures, winds, and sea level over the northeast Pacific continental shelf: 35°N to 48°N, *J. Geophys. Res., 92,* 1507-1526, 1987.

Syvitski, J. P., and M. D. Morehead, Estimating river-sediment discharge to the ocean: Application to the Eel margin, northern California, *Mar. Geol., 154,* 13-28, 1999.

Wallcraft, A. J., The Navy layered ocean model user's guide, *NOARL Rep. 35,* 27 pp., Nav. Res. Lab., Stennis Space Center, Miss., 1991.

Wheatcroft, R. A., C. K. Sommerfield, D. E. Drake, J. C. Borgeld, and C. A. Nittrouer, Rapid and widespread dispersal of flood sediment on the northern California margin, *Geol., 25,* 163-166, 1997.

J. S. Allen, College of Oceanic and Atmospheric Sciences, Oregon State University, Corvallis, OR 97331, USA. (jallen@oce.orst.edu)

J. D. Pullen, Marine Meteorology Division, Naval Research Laboratory, 7 Grace Hopper Avenue, Monterey, CA 93943, USA. (pullen@nrlmry.navy.mil)

(Received July 12, 2000; revised April 11, 2001; accepted April 27, 2001.)